



Review

A Narrative Review of Image Processing Techniques Related to Prostate Ultrasound



Haiqiao Wang^{a,b}, Hong Wu^a, Zhuoyuan Wang^a, Peiyan Yue^a, Dong Ni^a, Pheng-Ann Heng^b, Yi Wang^{a,*}

^a Medical UltraSound Image Computing (MUSIC) Lab, Smart Medical Imaging, Learning and Engineering (SMILE) Lab, School of Biomedical Engineering, Shenzhen University Medical School, Shenzhen University, Shenzhen, China

^b Department of Computer Science and Engineering, The Chinese University of Hong Kong, Hong Kong, China

ARTICLE INFO

Keywords:

Transrectal ultrasound
Prostate cancer
Medical image processing
Deep learning
Machine learning
Medical image segmentation
Medical image registration
Classification
Computer-assisted detection
Computer-assisted diagnosis

ABSTRACT

Prostate cancer (PCa) poses a significant threat to men's health, with early diagnosis being crucial for improving prognosis and reducing mortality rates. Transrectal ultrasound (TRUS) plays a vital role in the diagnosis and image-guided intervention of PCa. To facilitate physicians with more accurate and efficient computer-assisted diagnosis and interventions, many image processing algorithms in TRUS have been proposed and achieved state-of-the-art performance in several tasks, including prostate gland segmentation, prostate image registration, PCa classification and detection and interventional needle detection. The rapid development of these algorithms over the past 2 decades necessitates a comprehensive summary. As a consequence, this survey provides a narrative review of this field, outlining the evolution of image processing methods in the context of TRUS image analysis and meanwhile highlighting their relevant contributions. Furthermore, this survey discusses current challenges and suggests future research directions to possibly advance this field further.

Introduction

Prostate cancer (PCa) is a malignant disease of the prostate gland. According to [1,2], in 2022, the number of patients with PCa ranked second among male cancer patients worldwide, accounting for 14.2%, and the number of deaths from PCa ranked fifth among male cancer patients, accounting for 7.3%. Early diagnosis and treatment is the crucial key to the cure of progressive PCa. If this cannot be carried out effectively, PCa can invade nearby tissues and spread to other parts of the body, such as bones, seminal vesicles and the rectum [3]. Such spread not only severely affects the patient's quality of life but also increases the risk of death. The prevalence of subclinical and undiagnosed PCa is high among elderly men, and the incidence of asymptomatic PCa is also significant. Approximately one-half of patients with low-risk PCa (Gleason score of ≤ 6 /Grade Group 1) ultimately require active treatment. For low-risk PCa, more active monitoring is an effective approach [4]. Therefore, early diagnosis of PCa is crucial for improving the treatment success rate and reducing mortality.

The diagnostic procedure for PCa requires the comprehensive use of various detection tools to ensure accuracy. First, digital rectal examination is a traditional method for preliminary assessment of the prostate condition, where the size, shape and texture of the prostate are checked through rectal palpation [5]. Second, prostate-specific antigen (PSA)

blood testing is an important screening tool that assesses the risk of prostate disease by measuring the level of PSA in the blood, despite the possibility of its elevation owing to non-cancerous reasons [6]. Additionally, imaging examinations, including ultrasound examination, computed tomography (CT) scans and magnetic resonance imaging (MRI), provide physicians with more detailed views of the prostate structure [7], with multi-parametric MRI offering higher resolution images that help to locate tumors more accurately. Ultimately, prostate biopsy is a key step in confirming PCa, determining the nature of the tumor through pathological analysis. However, early cancerous lesions are often small and difficult to accurately locate and obtain sufficient samples in one biopsy, usually requiring multiple attempts. Multiple biopsies not only increase patient discomfort but can also lead to complications such as prostatitis or urinary tract infections [8]. To reduce this over-diagnosis phenomenon, additional imaging guidance for targeted prostate biopsy is essential [9], such as MRI and ultrasound examination.

Transrectal ultrasound (TRUS)-guided prostate biopsy is the standard method for the diagnosis of PCa, which is widely used in clinical practice [10]. TRUS scans the prostate through the rectal wall, generating images of the prostate, including B-mode, micro-ultrasound (micro-US), color Doppler ultrasound examination, contrast-enhanced ultrasound (CEUS) examination, 3-D imaging and elastography, to meet various clinical needs. The real-time B-mode provides two-dimensional

* Corresponding author. Room 510, A2 Building, Shenzhen University (Lihu Campus), Shenzhen, 518060, China.

E-mail address: onewang@szu.edu.cn (Y. Wang).

images commonly used for the diagnosis of benign prostate hyperplasia and prostatitis and intraoperative guidance. Although 3-D TRUS generates comprehensive 3-D volumetric information that is particularly important for preoperative planning. Furthermore, micro-US operates at a higher frequency than conventional ultrasound, providing higher-resolution imaging. However, this technology is not yet widely available, and there is limited imaging processing research related to it. CEUS and color Doppler ultrasound examination are used to identify suspicious regions based on the assumption that microvascular density increases in PCa owing to its association with angiogenesis. These imaging techniques can easily detect areas with dense blood vessels, assisting clinicians in quickly identifying suspicious vascular regions [11]. Elastography, in contrast, relies on the assumption that PCa regions tend to exhibit increased stiffness, often owing to higher cell density, which reduces tissue elasticity. These stiffened areas can be detected by strain elastography or shear wave elastography (SWE), enabling clinicians to locate potential regions of concern based on increased tissue hardness. However, using these two modalities alone to localize PCa can lead to false positives. Prostatitis and benign prostate hyperplasia can also cause increased vascularization, and benign nodules and prostate fibrosis can result in tissue stiffening. Therefore, it is essential for clinicians to integrate information from multiple modalities to localize PCa accurately [12].

Here are several key clinical tasks where TRUS is needed as an imaging tool for the diagnosis and treatment of PCa.

PCa classification and detection

TRUS can help physicians identify different types of PCa, including localized and invasive PCa. Through TRUS images, physicians can roughly assess the size, location and invasion of tumors into surrounding tissues.

Prostate gland segmentation

Accurate prostate boundary delineation from TRUS images can provide the target area for interventions, which facilitates physicians with effective treatment planning, biopsy needle placement and brachytherapy.

Image guidance for prostate intervention

TRUS is the routine imaging tool for image-guided biopsy and therapy of PCa, owing to its real-time advantage. Moreover, other preoperative imaging modalities such as MRI can be registered/fused with TRUS to provide more comprehensive visual information, thereby improving the efficacy of the intervention.

Intraoperative needle localization

During the procedure of biopsy, brachytherapy, cryotherapy and so on, TRUS is used to monitor the position of the biopsy or treatment needle, ensuring the accuracy and safety of the intervention.

Although TRUS has been widely used for the imaging of the prostate, there are still limitations in practical applications. The image quality may be degraded by speckle noise and shadow, leading to blurred details and artifacts. Especially in the apex and base regions of the prostate, the gland's contour in TRUS is often unclear, increasing the complexity of diagnosis. In addition, the interpretation of TRUS depends on the experience and skill of the physicians, leading to subjectivity. Moreover, the modalities and dimensions of TRUS are various, making it difficult for physicians to quickly obtain potentially useful information during diagnosis and treatment. Therefore, applying image processing technology to analyze TRUS is with clinical significance.

The development of image processing technology has greatly promoted the progress of the medical imaging field [13–15], especially playing an important role in computer-assisted diagnosis and computer-assisted intervention. With the help of advanced image processing methods, it is beneficial for physicians to make more accurate and efficient clinical decisions. In the field of TRUS image processing, lots of relevant methods have been developed and applied in different tasks, mainly including prostate gland segmentation, prostate image registration, PCa classification and detection and interventional needle detection, as illustrated in Figure 1.

This survey summarizes the related image processing methods in TRUS over the past 20 years, including gland segmentation, image registration, PCa classification and detection and interventional needle detection. We classify and summarize these methods according to modality,

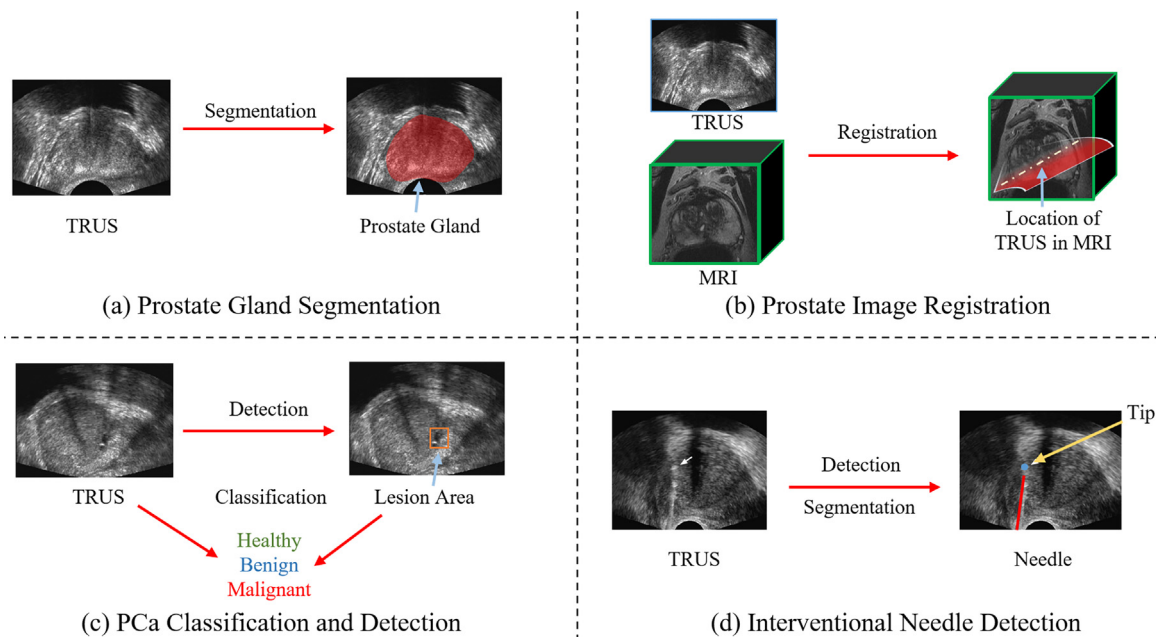


Figure 1. Illustration of conventional image processing tasks on transrectal ultrasound (TRUS), including (a) prostate gland segmentation, (b) prostate image registration, (c) prostate cancer (PCa) classification and detection, and (d) interventional needle detection.

dimension and technical route, presenting the similarities and differences of these methods. We also list the primary evaluation metrics for different tasks, as well as the results of representative methods under their datasets and metrics, making a rough comparison of different methods. Finally, we also summarize these methods to propose current challenges faced by each task and possible future research directions.

The organization of this survey is as follows. In the Task Definition section, we define each task of TRUS image processing and list the definitions and formulas of their primary evaluation metrics. The Method Overview section is the main part of this survey, where we review and summarize the methods of prostate gland segmentation, prostate image registration, PCA classification and detection and needle detection in the Prostate Gland Segmentation section, Prostate Image Registration section, Prostate Cancer Classification and Detection section and Needle Detection section, respectively. In the Discussion and Future Research Directions section, we discuss and analyze existing challenges and suggest future research directions for these four tasks. A summary of the entire survey is provided in the Summary.

Task Definition

Prostate Gland Segmentation

Image segmentation is one of the most common tasks in the field of medical image processing. The purpose of prostate segmentation is to accurately obtain the contour/region of the prostate gland (see Fig. 1a). Prostate segmentation plays a crucial role in different stages of the clinical decision-making process. For example, prostate volume, which can be directly determined through prostate segmentation, aids in the diagnosis of benign prostate hyperplasia. Moreover, the boundary information of the prostate is important and useful in various treatment scenarios, such as prostate brachytherapy, high-intensity focused ultrasound therapy, cryotherapy and transurethral microwave therapy. In addition, prostate segmentation also facilitates other image processing tasks, such as surface-based multi-modality image registration. To achieve prostate segmentation, lots of shape-/region-based methods, as well as conventional machine learning methods and advanced deep learning (DL) methods, have been developed. We classify and summarize these segmentation methods in the Prostate Gland Segmentation section, according to TRUS modality, dimension and technical route.

Evaluation Metrics

The evaluation of segmentation accuracy can be divided into qualitative and quantitative evaluations. For qualitative evaluation, the resulting contours are visually compared to the ground truth. For quantitative evaluation, the numerical calculation involves measuring the similarity between the obtained contours and the ground truth. The commonly used quantitative evaluation metrics consist of region-based metrics, boundary-based metrics and classification-based metrics. Because traditional segmentation methods often rely on contour constraints, they always use boundary-based metrics for the evaluation. In contrast, recent DL methods usually use region-based metrics.

The Dice similarity coefficient (DSC) is currently the most popular region-based evaluation metric for the segmentation task, which measures the overlap between the segmented result and the ground truth:

$$DSC = \frac{2 \times TP}{FP + FN + 2 \times TP}, \quad (1)$$

where TP , FP and FN denote true-positive, false-positive and false-negative regions, respectively.

Intersection over union (IoU) is another commonly used region-based metric, also known as the Jaccard coefficient. It is defined as follows:

$$IoU = \text{Jaccard} = \frac{TP}{TP + FP + FN}. \quad (2)$$

Larger values of DSC and IoU indicate better segmentation accuracy.

As for the boundary-based metrics, mean surface distance (MSD), mean absolute distance (MAD) and average symmetric surface distance (ASD) are often used to measure the similarity between the segmented boundary (in 2-D)/surface (in 3-D) and the ground truth:

$$MSD = \frac{1}{N} \sum_{i=1}^N d_i, \quad (3)$$

$$MAD = \frac{1}{N} \sum_{i=1}^N |d_i|, \quad (4)$$

$$ASD = \frac{1}{N} \sum_{i=1}^N (|d_i| + |d'_i|), \quad (5)$$

where N is the total number of points from the segmented boundary/surface, d'_i represents the shortest distance from the i -th point on the segmentation result to the ground truth and d_i represents the shortest distance from the i -th point on the ground truth to the segmentation result. It can be seen that MSD, MAD and ASD measures the average distance, mean absolute distance and average symmetric distance, respectively.

In contrast with the MSD, MAD and ASD, the maximum distance (MAXD) and Hausdorff distance (HD) are used to represent the dissimilarity between the segmented boundary/surface and the ground truth:

$$MAXD = \max |d_i|, \quad (6)$$

$$HD = \max(\max |d_i|, \max |d'_i|). \quad (7)$$

The MAXD measures the maximum distance between each point from the segmentation result and its corresponding point from the ground truth. The HD measures the maximum distance between the segmentation result and ground truth, and with 95HD denoting the 95th percentile of HD. For all aforementioned boundary-based metrics, smaller values denotes better segmentation accuracy.

In addition to region- and boundary-based metrics, point-wise classification-based metrics can also be applied to measure segmentation accuracy. Accuracy represents the proportion of correctly predicted pixels to the total number of pixels in the segmentation result:

$$ACC = \frac{TP + TN}{TP + TN + FP + FN}, \quad (8)$$

where TN denotes true negative. Sensitivity and recall indicate the proportion of all positive pixels that are correctly segmented as true positive:

$$\text{Sensitivity} = \text{Recall} = \frac{TP}{TP + FN}. \quad (9)$$

Precision indicates the proportion of all predicted positive pixels that are TP pixels:

$$\text{Precision} = \frac{TP}{TP + FP}. \quad (10)$$

There is usually a trade-off between precision and sensitivity. Specificity is the proportion of all negative pixels that are correctly segmented as true negative:

$$\text{Specificity} = \frac{TN}{TN + FP}. \quad (11)$$

Larger values of these classification-based metrics indicate better segmentation.

Prostate Image Registration

Image registration is the process of aligning two or more images acquired at varying times or viewpoints or by different sensors. Taking registering a pair of images as an example, one is denoted as fixed image and the other as a moving image. The objective is to estimate the

optimal deformation field between the fixed and moving images; thus, the warped moving image can be matched with the fixed image, enabling the alignment of the regions of interest. Prostate image registration plays a crucial role in assisting surgeons during preoperative planning and intraoperative surgery, with TRUS being a frequently used modality in this context. Its purpose is to provide surgeons with more complementary and valuable information. This task often involves analyzing multi-modality images (e.g., MR to TRUS) (see Fig. 1b), and thus remaining challenging in clinical practice. We classify and summarize relevant registration methods in the Prostate Image Registration section, according to modality, dimension, deformation type and technical route.

Evaluation Metrics

Considering the purpose of image registration, the numerical evaluation metrics are mainly aimed at quantifying the similarity of corresponding regions between the fixed image and the warped moving image. Therefore, the metrics like DSC, HD, MAD and MAXD can also be used to evaluate the registration performance, by calculating the overlap of corresponding regions or the distance of corresponding boundaries pr surfaces.

Target registration error (TRE) is one of the most commonly used metrics in medical image registration. It involves measuring the Euclidean distance of the manually identified corresponding landmarks in the fixed and moving images:

$$TRE = \frac{1}{N} \sum_{i=1}^N \|L_{I_f}^i, L_{I_m}^i \circ \phi\|_2, \quad (12)$$

where L denotes the landmark set, and N is the total number of corresponding landmark pair in L . I_f and I_m are the fixed and moving images, respectively. ϕ is the estimated deformation field, and \circ denotes the warping operation. $\|\cdot\|_2$ is the L2 norm.

Surface registration error (SRE) has a similar computing method with TRE, but the difference is SRE measures the similarity of surface points between fixed and moving images:

$$SRE = \frac{1}{N} \sum_{i=1}^N \|S_{I_f}^i, S_{I_m}^i \circ \phi\|_2, \quad (13)$$

where S denotes the prostate surface point set, and N is the total number of corresponding point pair in S . Smaller values of TRE and SRE indicate better registration accuracy.

In addition to assessing registration accuracy using these metrics, some studies also evaluate the quality of the estimated deformation field ϕ . The Jacobian matrix $J_\phi(p) = \nabla \phi(p)$ evaluates the regularity of the deformation field by capturing the local gradient of ϕ around pixel p . A smaller value of the percentage of pixels with non-positive Jacobian determinant ($\% |J_\phi| \leq 0$) indicates a smoother ϕ .

PCa Classification and Detection

Early and accurate diagnosis, along with precise staging, effectively improves the success rate of treatment. The standard method for diagnosing and grading PCa is the histopathological analysis of prostate tissue samples, typically obtained via TRUS-guided biopsy. Consequently, the accurate identification of target lesions during the biopsy procedure has been a longstanding and active research task. To better support TRUS-guided targeted biopsies, automated detection methods have been developed to predict PCa based on TRUS images (Fig. 1c). Most of these methods approach cancer detection as a classification problem, where small regions of interest or whole images are categorized as benign or malignant. We classify and introduce these methods in the Prostate Cancer Classification and Detection section, according to TRUS modality and technical route.

Evaluation Metrics

The evaluation metrics for classification task mainly include area under the receiver operating characteristic curve, accuracy (8), sensitivity (9), specificity (11), precision (10) and F-score.

The area under the receiver operating characteristic curve is a measure of the diagnostic ability of a binary classifier, which computes the area under the receiver operating characteristic curve. The receiver operating characteristic curve is a curve drawn with the true-positive rate (namely, sensitivity) as the y axis and the false-positive rate (namely, specificity) as the x axis. The area under receiver operating characteristic curve can be calculated as:

$$AUC = \int_0^1 TPR(fpr) dfpr. \quad (14)$$

It represents the probability that a randomly chosen positive instance is ranked higher than a randomly chosen negative instance.

The F-score is a weighted harmonic mean of precision and recall:

$$F\text{-score} = 2 \times \frac{\text{Precision} \times \text{Recall}}{\text{Precision} + \text{Recall}}. \quad (15)$$

Needle Detection

Prostate needles are primarily used during surgical procedures for various purposes, including biopsy, brachytherapy, high-intensity focused ultrasound therapy, cryotherapy and so on. Automated detection and segmentation of interventional needles are crucial in surgical settings because this ensures precise localization and safe interventions, as illustrated in Figure 1d. We summarize needle detection methods in the Needle Detection section, according to clinical scenario and technical route.

Evaluation Metrics

The numerical metrics for evaluating the needle detection and segmentation mainly include shaft error and tip error. Shaft error measures the deviation between the predicted and actual axes of the needle, usually expressed in terms of distance or angle:

$$E_{shaft}^{distance} = \frac{1}{N} \sum_{i=1}^N \|\mathbf{o}_i, \hat{\mathbf{o}}_i\|_2, \quad (16)$$

$$E_{shaft}^{angle} = \arccos\left(\frac{\mathbf{v} \cdot \hat{\mathbf{v}}}{\|\mathbf{v}\| \|\hat{\mathbf{v}}\|}\right), \quad (17)$$

where N is the number of points in a needle, $\hat{\mathbf{o}}_i$ represents the predicted position for the i -th point, and \mathbf{o}_i is the ground truth position for the of the i -th point. \mathbf{v} and $\hat{\mathbf{v}}$ represent the actual and predicted axis direction vectors.

Tip error measures the difference between the predicted and actual tip positions of the needle:

$$E_{tip} = \|\mathbf{t}, \hat{\mathbf{t}}\|_2, \quad (18)$$

where \mathbf{t} and $\hat{\mathbf{t}}$ represent coordinates of the actual and predicted needle tip.

Method Overview

In this section, we provide an overview of the key technologies involved in the four tasks of TRUS prostate imaging analysis.

Prostate Gland Segmentation

Modalities

Multi-modality TRUS images including B-mode, color Doppler, elastography and micro-US examination have been used for the diagnosis of PCa. Each modality offers unique insights into the physiological and pathological states of the diseases. Among the TRUS modalities, the B-

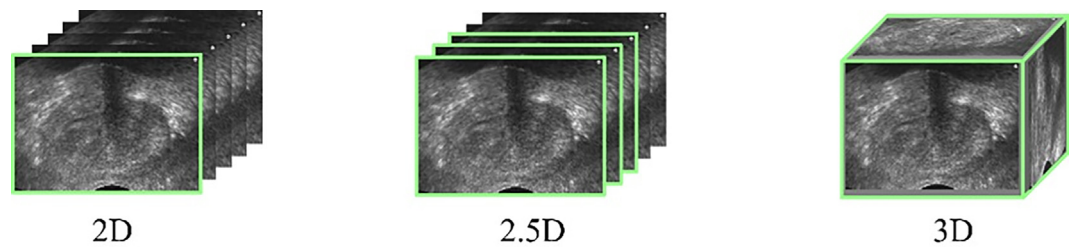


Figure 2. Illustration of different dimensions of the input images for the processing algorithms. The fluorescence indicates the field of view (FOV) handled by the algorithm in a single pass.

mode ultrasound examination is predominantly used for prostate segmentation. The B-mode TRUS affords a morphological representation of the prostate, thereby facilitating the accurate delineation of the prostate’s contour.

Almost all segmentation studies mentioned in this survey used B-mode TRUS for the prostate segmentation. Few studies used multi-modality TRUS or high-resolution micro-US. Mahdavi et al. [16] boosted the performance of B-mode TRUS segmentation by offering supplementary information from the vibro-elastography images. Jiang et al. [17] and Zhang et al. [18] segmented prostate gland from the micro-US images. Their research has underscored the potential of this high-resolution modality in the precise segmentation of the prostate.

Dimensions

We categorize prostate segmentation approaches as 2-D, 2.5-D or 3-D methods, according to the TRUS dimension they processed. Note that 2-D and 3-D algorithms process one slice and a whole volume, respectively, whereas 2.5-D processes several consecutive 2-D slices (Fig. 2). As shown in Table 1, the majority of researches have concentrated on 2-D and 3-D techniques, with a comparatively modest exploration of the 2.5-D methodology.

The 2-D segmentation is executed on an individual slice of the prostate image. This approach is frequently used for intraoperative real-time navigation, serving to assist clinicians in the precise identification of the prostate gland’s location and boundary. The merits of 2-D segmentation include its simplicity and high computational efficiency. Nonetheless, it falls short in capturing the 3-D morphology of the prostate, potentially leading to inaccuracies in the volumetric assessment of the prostate, particularly concerning the apex and base regions.

In contrast with 2-D segmentation, 3-D segmentation is conducted on the entire volumetric TRUS data. This technique is used predominantly in preoperative planning, aiding physicians in delineating the extent and trajectory for surgical excision or in radiation therapy planning by enabling radiation oncologists to pinpoint the target region for irradiation. Importantly, 3-D segmentation affords an exhaustive and accurate quantitative analysis of the prostate’s shape, volume and boundaries. However, it is encumbered by high computational demands and necessitates the processing of a vast array of voxels and intricate 3-D structures.

Beyond the 2-D and 3-D approaches, the 2.5-D segmentation technique operates on multiple contiguous slices of the prostate image. By integrating information from multiple slices, 2.5-D segmentation can partially capture the volumetric information. It offers an advantage over

2-D segmentation in better handling the 3-D morphological variations of the prostate, albeit with limitations imposed by the selection and thickness of the slices. Compared with 3-D segmentation, 2.5-D segmentation can alleviate the computational load, presenting a more efficient compromise between computational demands and segmentation accuracy.

Segmentation Methods

We categorize prostate segmentation methods into two ways: traditional methods and DL methods. Table 2 shows the categorization in detail. It can be seen that, before 2016, almost all of the studies were about traditional methods; thereafter, DL methods dominated this area.

Traditional Methods. We present the traditional methods for prostate segmentation in four categories: contour- and shape-based methods, region-based methods, conventional machine learning methods and hybrid methods. Such categorization is determined on the underlying theoretical computational approaches used to address the segmentation task. Table 3 gives a comprehensive summary of the representative studies using traditional methods for TRUS segmentation.

Contour- and shape-based methods. These methods use prostate contour and edge information to guide the segmentation. Contour-based methods typically initiate with edge detection. [19] introduced a Sticks algorithm to enhance contrast and reduce speckle noise in TRUS examination, thus facilitating the rendering of prostate edges as a visual guide for subsequent edge detection and manual refinement. Shen et al. [20] expanded on this by using a Gabor filter bank to characterize prostate boundary features across multiple scales and orientations, followed by a hierarchical deformation strategy to adaptively focus on feature similarity. This approach, while more time-consuming, captured a broader range of boundary directions. Wu et al. [21] diverged from the traditional view by leveraging speckles’ intrinsic properties to aid segmentation, arguing that speckle characteristics provide useful cues for prostate boundary delineation.

Active shape models (ASM), as pioneered by [22], offer a statistical shape-based method that has been further developed by researchers such as [23], who presented a robust automatic initialization of the ASM for prostate. This method used pixel classification for the initialization of prostate region and a multi-population genetic algorithm for ASM pose adjustment. Mahdavi et al. [16] and Bi et al. [24] extended the ASM by incorporating high-contrast vibro-elastography images and clustering techniques using a Rayleigh mixture model, respectively, to enhance the initialization and deformation guidance of the ASM model.

Beyond ASM, other shape-prior-based segmentation techniques have been explored. Badiei et al. [25] proposed an image warping technique to impose an elliptical shape on the prostate, with subsequent optimization of the elliptical fitting using boundary points from an edge detector. Mahdavi et al. [26] further advanced this by suggesting twisted and tapered ellipsoids as suitable a priori 3-D shapes, transforming the shape fitting into a convex problem for efficient solution. Yen et al. [27] proposed adaptive learning of local neighborhood shape statistics to capture patient-specific variations. Qiu et al. [28] introduced a semi-automatic method integrating shape constraints with a modified level set

Table 1
Prostate segmentation approaches categorized as 2-D, 2.5-D, and 3-D methods.

Dimensions	References
2-D	[17,19–21,23–25,27,35,36,38,39,42,44,49,50,57,58,60,62,64,137–197]
2.5-D	[63,198,199]
3-D	[16,18,26,28–34,37,40,41,43,45,46,48,51–56,61,158,200–213]

Table 2

Traditional segmentation methods and deep learning methods. Traditional methods can be categorized as contour/shape based methods, region based methods, conventional machine learning methods, and hybrid methods. DL methods mainly apply CNN, RNN, and attention enhanced networks.

Classifications	References
Contour/shape-based methods	[16,19–21,23–28,138–141,143–146,150,151,153,154,156,163,164,166,170,172,173,187,200–202,204,209,214]
Region-based methods	[29–34,157,165,171,207,210]
Conventional machine learning methods	[35–39,137,147,152,155,162,180,183–186,188,189,192,193,195,197,206,208]
Hybrid methods	[40–44,46,142,147–149,158–161,167,168,175,203,205,207]
CNN	[17,18,48–56,174,177,178,181,182,190,194,196,198,199,212]
RNN	[57,58]
Attention enhanced network	[60–64,179,213]

CCN, convolutional neural network; RNN, recurrent neural network.

Table 3

Overview of traditional methods for prostate gland segmentation in transrectal ultrasound

Traditional Methods	References	Dimension	Auto/Semi-auto	Methods	Samples	Results	
						Metrics	Values
Contour and shape	[19]	2-D	Semi-auto	Probabilistic filters, edge detection, manual editing	125	MAD	0.7 ± 0.4 mm
						HD	1.8 ± 1.0 mm
	[20]	2-D	Automatic	Gabor filter bank, statistical shape model	8	1-DSC	$1.66 \pm 1.68\%$
						1-IoU	$3.98 \pm 0.97\%$
						MAD	3.20 ± 0.87 pixels
	[25]	2-D	Semi-auto	Image warping, edge detection, ellipse fitting	17	MAD	0.67 ± 0.18 mm
						MAXD	2.25 ± 0.56 mm
	[23]	2-D	Automatic	Pixel classification, active shape model	22	MAD	1.74 ± 0.69 mm
						MAXD	4.51 ± 2.42 mm
	[26]	3-D	Semi-auto	Shape fitting, convex optimization	40	1-DSC	$5.82 \pm 4.15\%$
	[28]	3-D	Semi-auto	Shape constraint, level set	20	DSC	$93.39 \pm 1.26\%$
						MAD	1.16 ± 0.34 mm
Region	[16]	3-D	Automatic	Elastography, active shape model	11	DSC	$87 \pm 7\%$
	[21]	2-D	Automatic	Rotation-invariant texture feature, graph cut, level set	598	MAD	1.06 ± 0.53 mm
	[24]	2-D	Automatic	Rayleigh mixture model, active shape model	30	DSC	$95 \pm 0.81\%$
						MAD	1.86 ± 0.02 pixels
	[29]	3-D	Semi-auto	Region information, level set	8	Visual comparison	Visual comparison
	[30]	3-D	Automatic	Rotational symmetry, convex optimization	20	DSC	$93.7 \pm 2.1\%$
						MAD	1.12 ± 0.4 mm
						MAXD	3.15 ± 0.65 mm
	[33]	3-D	Automatic	Multi-atlas fusion, pairwise shape similarity	50	DSC	$92.08 \pm 1.96\%$
						MAD	1.22 ± 0.57 mm
	[32]	3-D	Automatic	Volume-preserving prior, convex optimization	12	MAXD	3.47 ± 1.48 mm
						DSC	$89.5 \pm 2.4\%$
Machine learning						MAD	1.4 ± 0.6 mm
						MAXD	5.2 ± 3.2 mm
	[31]	3-D	Automatic	Axial symmetry, convex optimization	25	DSC	$93.2 \pm 2.0\%$
	[34]	3-D	Automatic	Multi-atlas fusion, atlas agreement factor	280	DSC	$89.75 \pm 3.75\%$
						MSD	1.33 ± 0.60 mm
	[35]	2-D	Automatic	Statistical shape and appearance model, random forest	126	DSC	$91 \pm 4\%$
						MAD	1.30 ± 0.3 mm
	[36]	2-D	Automatic	Sparse dictionary learning	590	HD	3.62 ± 0.56 mm
						MSD	0.98 ± 0.39 mm
	[37]	3-D	Automatic	Kernel SVM	10	HD	5.4 ± 1.38 mm
	[38]	2-D	Semi-auto	Improved closed principal curve	50	DSC	$89.7 \pm 2.3\%$
						DSC	96.5%
Hybrid						Jaccard	95.1%
						ACC	96.3%
	[39]	2-D	Semi-auto	Adaptive polygon tracking model, principal curve	1320	DSC	$96.4 \pm 2.4\%$
						Jaccard	$95.5 \pm 2.9\%$
						ACC	$96.1 \pm 2.5\%$
	[40]	3-D	Automatic	Kernel SVM, statistical shape model	3	1-IoU	3.9%
						MAD	0.81 voxel
	[42]	2-D	Automatic	Deformable superellipses, Bayesian model	125	MAD	1.36 ± 0.58 mm
						HD	3.42 ± 1.52 mm
	[43]	3-D	Semi-auto	Spherical harmonics, statistical analysis	30	MAD	1.26 ± 0.41 mm
						MAXD	4.06 ± 1.25 mm
	[41]	3-D	Automatic	Gabor-SVM, statistical texture matching	5	1-IoU	$4.31 \pm 0.40\%$
						MAD	1.07 ± 0.10 voxels
	[44]	2-D	Automatic	Partial active shape model, region model	301	MAD	2.01 ± 1.02 mm
	[45]	3-D	Semi-auto	Discrete dynamic contour, optimal surface detection	28	ASD	0.77 ± 0.28 mm
	[46]	3-D	Automatic	Hybrid edge/region-based parametric deformable model	36	DSC	$92 \pm 2\%$
						MAD	1.42 ± 0.40 mm
						HD	4.03 ± 1.22 mm

ACC, accuracy; DSC, dice similarity coefficient; HD, Hausdorff distance; IoU, intersection over union; MAD, mean absolute distance; MAXD, maximum distance.

formulation for 3-D segmentation. These methods emphasized the importance of integrating shape priors with computational strategies to improve accuracy and efficiency.

Region-based methods. These methods harness local intensity values or statistical measures within an energy minimization framework to achieve segmentation. Fan et al. [29] initially developed a fast discrimination technique for extracting the prostate region and subsequently addressed the “boundary leaking” issue by integrating regional information, rather than gradient information, into the level set method. Yuan et al. [30] used rotationally re-sliced images around a specified axis to delineate 3-D prostate boundaries, a technique that effectively capitalized on the inherent rotational symmetry of prostate shapes to adjust a series of 2-D slice segmentation in a unified 3-D context. The work [30] was further extended to [31], with more validation data. Qiu et al. [32] introduced a convex optimization strategy for extracting the prostate surface, while maintaining the global volume size prior. Moreover, they implemented an efficient numerical solver on graphics processing units (GPUs). Additionally, some methods accomplish the extraction of the prostate region through template matching. Nouranian et al. [33] designed a multi-atlas fusion framework to segment TRUS images using pairwise atlas shape similarity. Nouranian et al. [34] further introduced the atlas agreement factor to boost the robustness of the previous work [33]. This factor was integrated into an atlas selection algorithm to refine the dataset before merging the atlas contours, yielding consistent segmentation.

Conventional machine learning methods. Early prostate segmentation methods also encompass machine learning approaches. These techniques leverage features such as intensity or higher-dimensional attributes like filter responses to cluster and/or classify the image into prostate and background regions. Ghose et al. [35] introduced a method for prostate segmentation that constructed a multiple average parameter model derived from the principal component analysis of shape and a posterior probabilities within a multi-resolution framework. The model parameters were subsequently refined using a priori knowledge of the optimization space to achieve optimal prostate segmentation. Nouranian et al. [36] proposed a learning-based multi-label segmentation algorithm. A sparse representation method was integrated into the algorithm to learn a dictionary encoding information of images as well as clinical and planning target volume segmentation. Yang et al. [37] developed a block-based feature learning framework, where patient-specific anatomical features extracted from aligned training images served as signatures for each voxel. A feature selection process identified the most robust and informative features to train a kernel support vector machine (SVM).

Additionally, some methods have used the principal curve, which provided a means of representing low-dimensional data manifolds in high-dimensional spaces, thereby effectively capturing the complexity of prostate shapes. Peng et al. [38] proposed an improved closed principal curve approach, using only a few seed points defined by radiologists as an approximate initialization. Peng et al. [39] further developed an adaptive polygon tracking model to alleviate the issue of determining the segment number of the principal curve automatically. In addition, an interpretable mathematical function was formulated to constrain a smooth boundary.

Hybrid methods. The objective of hybrid methods is to leverage advantages from contour, shape, region and conventional machine learning to achieve better segmentation results. Zhan et al. [40] combined kernel SVM and statistical shape model (SSM) to segment 3-D TRUS. The kernel SVM was used to classify the prostate from surrounding tissues, and then the SSM was used to refine the contour. Later, Zhan et al. [41] improved on their earlier work [40] by using a set of Gabor-SVMs and the statistical texture matching model. Gong et al. [42] emphasized that the prior knowledge of prostate shapes played an important role for reliable segmentation. They used deformable super-ellipses to model the shape of prostate and further developed a robust Bayesian segmentation approach. Tutar et al. [43] used the eighth spherical harmonic function to depict the shape of the prostate, and

statistically analyzed the shape parameters. Yan et al. [44] used partial ASM and region model to address the issue of missing boundaries in shadow areas. Garnier et al. [45] sequentially combined discrete dynamic contour and optimal surface detection for semi-automatic 3-D TRUS segmentation in high-intensity focused ultrasound therapy. Jaouen et al. [46] proposed a hybrid edge and region-based parametric deformable model. The edge-based model was derived from the radial bas-relief approach, while the region-based model was regarded as a parametric active surface driven by the Bhattacharyya gradient flow.

DL methods. We categorize DL methods for TRUS segmentation into three classes: convolutional neural network (CNN), recurrent neural network (RNN) and attention enhanced networks, according to their network structure. Owing to limited studies on Transformer currently in this field, relevant researches are included in the attention enhanced networks section. Table 4 summarizes representative studies related to the DL-based segmentation in TRUS.

CNNs. CNNs are among the most successful and widely used architectures in DL, particularly for computer vision tasks. Following the advent of U-net [47], a plethora of CNNs with encoder–decoder structures have been used for medical image segmentation. Several methods have sought to enhance segmentation performance by improving loss functions. For instance, Lei et al. [48] developed a multi-directional DL method to segment TRUS for US-guided radiation therapy. They combined binary cross-entropy loss and batch-based Dice loss into a staged hybrid loss function for deeply supervised training. Karimi et al. [49] improved the uncertain segmentation by incorporating prior shape information in the form of a statistical shape model. Karimi et al. [50] presented a loss function for training the segmentation network with the goal of directly reducing the HD.

Additionally, other methods have focused on the improvement of the network structures. Lei et al. [51] developed an anchor-free mask CNN that consisted of three subnetworks: a backbone, a fully convolutional one-state object detector and a mask head. Xu et al. [52] proposed a novel polar transform network to address the issue of difficult segmentation in the challenging base and apex regions. The proposed network represented the prostate shape in the polar coordinate space. This representation provided much denser samples of the prostate volume, thus facilitating the learning of discriminative features for accurate prostate segmentation. Wang et al. [53] combined CNNs and tokenized multi-layer perceptron with a pyramid structure and hybrid attention to enable real-time TRUS prostate segmentation, enhancing accuracy through boundary-constrained loss.

Furthermore, some studies have focused on fully using data information. Xu et al. [54] proposed a shadow-consistent semi-supervised segmentation method that included shadow augmentation and shadow dropout. Shadow augmentation enlarged training samples by including simulated shadow artifacts to the images, while shadow dropout enhanced the network to leverage neighboring high-quality pixels to infer boundaries. Orlando et al. [55] developed an automatic 3-D TRUS segmentation network, trained on a large, clinically diverse dataset with variable image quality. Li et al. [56] used a CNN for automatic localization, introduced semantic constraints to reduce noise and used bi-directional iteration with denoising for optimal prostate segmentation.

RNNs. RNNs are commonly used for processing sequential data, such as speech, text, videos and time series data. Unlike unidirectional feed-forward neural networks, RNNs are bidirectional neural networks, allowing the outputs of certain nodes to influence subsequent inputs from the same nodes. Their capability to process arbitrary input sequences using internal state, or memory, makes them suitable for tasks such as unsegmented, connected handwriting recognition or speech recognition.

In the context of TRUS segmentation, Yang et al. [57] first serialized static 2-D TRUS images into dynamic sequences and then predicted prostate shape by sequentially exploring the shape prior. Subsequently, to mitigate the bias caused by different serialization approaches, they used

Table 4
Overview of deep learning methods for prostate gland segmentation in TRUS

Deep Learning Methods	References	Dimension	Methods	Samples	Results	
					Metrics	Values
CNN	[48]	3-D	1) Multi-directional deeply supervised V-Net	44	DSC	92 ± 3%
			2) A hybrid loss with binary cross-entropy and batch-based Dice		MSD	0.60 ± 0.23 mm
					HD	3.94 ± 1.55 mm
	[49]	2-D	1) An adaptive sampling strategy to address difficult cases	675	DSC	93.9 ± 3.5%
			2) A CNN ensemble to identify uncertain segmentation		HD	2.7 ± 2.3 mm
			1) A loss function to reduce the HD		DSC	94.6 ± 4.1%
	[50]	2-D		2625	ASD	1.05 ± 0.46 mm
					HD	2.6 ± 1.8 mm
			2) Three methods to estimate HD		DSC	94 ± 3%
	[51]	3-D	1) An anchor-free mask CNN	83	DSC	94 ± 3%
					95HD	2.27 ± 0.79 mm
					DSC	89.97 ± 3.47%
RNN	[52]	3-D	1) Represent prostate shape in the polar coordinate space	315	ASD	1.30 ± 0.61 mm
			2) A centroid perturbed test-time augmentation strategy		HD	7.07 ± 3.19 mm
					DSC	91.60 ± 2.37%
	[54]	3-D	1) Shadow augmentation and shadow dropout	2423	ASD	1.02 ± 0.34 mm
			2) Semi-supervised Learning		HD	6.37 ± 2.36 mm
					DSC	94.0%
	[55]	2-D	1) Modified U-Net and U-Net + +	6721	MSD	0.90 mm
					HD	3.27 mm
					DSC	94.75 ± 2.27%
	[53]	2-D	1) Multilayer perceptron enhanced CNN network	240	HD	2.53 ± 1.60 mm
			2) Boundary loss		DSC	96.74%
			1) Initial localization by CNN networks		DSC	96.74%
Attention	[56]	2-D	2) semantic constraint and bidirectional segmentation	132	IoU	93.71%
	[57]	2-D	1) Serialize static TRUS images into dynamic	530	DSC	92.33%
			2) A multi-view shape fusion strategy		Recall	89.76%
			3) A multiscale auto-context scheme		Precision	95.19%
	[58]	2-D	1) Residual convolution in recurrent networks	3892	DSC	92.91 ± 2.74%
			2) Recurrent connections for deep network lay		HD	2.97 ± 1.96 mm
	[60]	2-D	1) Select useful complementary information from multi-level features to refine the features at each individual layer	530	DSC	95.27%
					Recall	96.98%
					Precision	93.69%
	[61]	3-D	1) Selectively leverage multi-level features from different layers	40	DSC	90 ± 3%
					Recall	91 ± 4%
					Precision	90 ± 6%
Attention	[62]	2-D	1) A channel-wise attention strategy	145	DSC	88 ± 3%
			2) Learning-based prior shape knowledge		95HD	2.01 ± 0.54 mm
					DSC	94.0 ± 3.0%
	[63]	2.5-D	1) Feature positioning information	2892	95HD	2.29 ± 1.45 mm
			2) A training scheme that uses knowledge distillation		DSC	94.3 ± 3.8%
					ACC	93.9 ± 4.1%
	[64]	2-D	1) Attention gate modules with squeeze-and-U-net	945	DSC	94.3 ± 3.8%
			2) An improved polygon searching model		ACC	93.9 ± 4.1%
			3) A storage-based quantum evolution model			
	[17]	2-D	1) An annotation-guided binary cross entropy loss	2060	DSC95HD	93.9%2.02 mm
					DSC	91.8 ± 3.1%
					ASD	1.18 ± 0.45 mm
	[18]	2-D	Swin Transformer enhanced Mask2Former network	13650	HD	3.28 ± 1.24 mm

ACC, accuracy; DSC, dice similarity coefficient; HD, Hausdorff distance; IoU, intersection over union; TRUS, transrectal ultrasound.

a multi-view fusion strategy to merge shape predictions obtained from various perspectives. Furthermore, they integrated the RNN core into a multi-scale automatic context scheme to continuously refine the details of the shape prediction graph. Similarly, Anas et al. [58] not only used CNNs to extract spatial features but also used RNNs to leverage the temporal information among a series of TRUS images. Additionally, they used cyclic connections within and between different layers of the network to maximize the utilization of temporal information.

Attention enhanced network. In DL methods, an attention block [59] can selectively modify inputs or assign different weights to input variables according to their varying importance. Attention mechanisms in DL are fundamentally analogous to the selective visual attention mechanisms in humans, with the core objective being to select the most critical information from a vast amount of data for the current task's goal.

In the context of TRUS segmentation, Wang et al. [60] first developed a network equipped with deep attentional feature modules to enhance segmentation by fully exploiting the complementary information encoded in different layers of the CNN. The deep attentional feature module selectively used multi-level features integrated across different

layers to refine each individual layer, suppressing non-prostatic noise in shallow layers of the CNN, and enriching deeper features with more prostatic detail. Further, Wang et al. [61] extended work by Wang et al. [60] to 3-D TRUS segmentation, by using more powerful backbone architecture. Girum et al. [62] presented a multi-task DL method for boundary detection in intraoperative TRUS, by leveraging both low-level and high-level information. The channel-wise attention strategy was used for low-level feature refinement, and the learning-based prior knowledge was used for high-level feature modeling. Vesal et al. [63] addressed the limitations of transfer learning and fine-tuning methods by introducing a 2.5-D deep neural network, which further relied on an attention module that considered feature positioning information to improve segmentation accuracy. Peng et al. [64] developed a coarse-to-fine architecture for TRUS segmentation. They used the attention gate module with squeeze-and-excitation U-net to conduct initial segmentation, and then jointly used a modified polygon-searching model and a storage-based quantum evolution model to refine the segmentation.

Some methods have also explored gland segmentation on micro-US using Transformer techniques. MicroSegNet [17], based on TransUNet

[65], used multi-scale deep supervision and an annotation-guided loss function to improve segmentation accuracy in difficult regions of the prostate on micro-US images. Zhang et al. [18] used a Swin Transformer [66] as the backbone and further leveraged [67] to achieve real-time prostate and central gland segmentation on micro-US images at 9 frames per second.

Prostate Image Registration

Modalities

Prostate image registration is useful for assisting surgeons during preoperative planning and intraoperative surgery. It can provide surgeons with more complementary information, especially the multi-modality registration. Table 5 lists the categorization of registration approaches according to the image modality. The majority of studies focused on MRI-TRUS registration, which registered the preoperative MRI scans to the TRUS images, providing better resolution and soft tissue contrast to assist targeted biopsy. In addition, CT-TRUS registration methods have also been investigated, mainly in the scenarios of treatment planning and prognosis evaluation. Other studies paid attention to the registration of preoperative and intraoperative TRUS images.

Dimensions

We classify registration methods into three categories based on dimensionality: 2-D–2-D, 2-D–3-D and 3-D–3-D, as shown in Table 6. Images acquired intraoperatively are predominantly 2-D TRUS, whereas those acquired preoperatively are mostly 3-D (MRI, CT and 3-D TRUS). Ultimately, the registration methods intended for prostate biopsy would necessitate the registration between intraoperative 2-D TRUS and preoperative 3-D images.

The process of registering 2-D TRUS to 3-D images from different modalities presents two main challenges: differing dimensions and distinct modalities. There was a scarcity of literature that addressed both of these issues simultaneously. Consequently, most 2-D–3-D studies concentrated on registration between TRUS images to bridge the dimensional gap, whereas 3-D–3-D studies primarily focused on registration between TRUS and other modalities to overcome the challenge posed by different imaging modalities.

Deformation types

According to different deformation types, we categorize the registration methods into linear and non-linear registration, as shown in Table 7. Rigid transformation, also referred to as isometric transformation, involves only translation and rotation. Affine transformation includes scaling and shear in addition to translation and rotation, making linear transformation a special case of affine transformation. In this survey, both rigid and affine transformations are uniformly classified as the category of linear registration. In contrast, non-linear registration refers to methods that go beyond linear registration, primarily involving deformable transformation. Unlike linear registration, deformable registration methods use non-linear dense transformation to align images. Most of prostate image registration methods focused on nonlinear registration to address the issue of large deformation in TRUS images.

Table 5
Prostate image registration studies categorized as TRUS-TRUS, MRI-TRUS, and CT-TRUS

Modalities	References
TRUS-TRUS	[69,72,73,87,88,215–220]
MRI-TRUS	[68,71,74,75,77–86,89–94,96–107,221–235]
CT-TRUS	[76,236–239]

CT, computed tomography; MRI, magnetic resonance imaging; TRUS, transrectal ultrasound.

Table 6

Prostate image registration studies categorized as 2-D–2-D, 2-D–3-D, and 3-D–3-D

Dimensions	References
2-D–2-D	[74]
2-D–3-D	[68,70,72,73,78,87,88,219,216,231,232,240]
3-D–3-D	[69,71,75,76,77,79–86,89–94,96–108,215,217,218,220–230,233–239]

Table 7

Prostate image registration studies categorized as linear registration and non-linear registration

Deformation Types	References
Linear	[68,72,73,86–89,91–94,103,219–221,236,240]
Non-linear	[69–71,74–85,90,97–102,104–108,215–218,222–235,237–239]

Registration methods

We categorize registration methods into two main types: traditional methods and DL methods, as shown in Table 8. Traditional methods, although often time consuming owing to the iterative estimation of the deformation field, are known for their stability and reliability across various scenarios. In contrast, DL methods have gained popularity owing to advancements in GPU computing power, enabling them to achieve more efficient registration than traditional methods.

Traditional methods. Traditional registration methods mainly investigated the following two aspects: matching criteria and deformation models. The matching criterion defines the similarity of the image pair, with intensity-based methods relying on the similarity of intensities or intensity-related features of images, and shape-based methods focusing on the similarity of prostate's region or boundary. The deformation model is also critical, as the registration process involves optimizing the parameters of the deformation fields to warp the moving image to match with the fixed image. We summarize the traditional registration methods on TRUS images according to different matching criteria.

Intensity-based methods. Table 9 summarizes some representative traditional registration methods, including intensity-based methods and shape-based methods. Xu et al. [68] used spatial tracking information to initialize the registration between intraoperative 2-D TRUS and preoperative 3-D TRUS. They then optimized the registration by calculating the grayscale similarity to eliminate spatial tracking errors. Additionally, they manually registered 3-D TRUS and 3-D MRI preoperatively, achieving a 2-D TRUS-3-D MRI registration process. Hungr et al. [69] used the correlation coefficient as a similarity metric to register 3-D TRUS, whereas Baumann et al. [70] used the shift correlation model combined with the inverse consistency constraint, performing linear registration separately from deformable registration. Sunet al. [71] used the modality-independent neighborhood descriptor as the local similarity feature

Table 8

Traditional registration methods and deep learning (DL) methods

	Classifications	References
Traditional methods	Intensity-based methods	[68–73,222,236]
	Shape-based methods	[74–85,215–217,221,223–230,237,238,240]
Deep learning methods	Image-based network	[86–94,96,218,219,231,235,239]
	Label-driven network	[97–104,220,232–234]
	Point set network	[105–108]

Traditional methods can be categorized as intensity-based methods and shape-based methods. DL methods mainly include image-based networks, label-driven networks, and point set networks.

Table 9
Overview of traditional methods for prostate TRUS registration

Traditional Methods	References	Dimensions Modalities	Deformation	Methods	Samples	Results	
						Metrics	Values: final (initial)
Intensity	[70]	2-D TRUS 3-D MRI	Non-linear	1) Shift correlation and inverse consistency 2) Local rigid and linear elastic deformation	40	TRE	0.8 ± 0.5 (13.8 ± 7.9) mm
	[72]	2-D TRUS 3-D TRUS	Linear	1) Optimize the normalized cross-correlation (NCC) metric using Powell's method	8	TRE	1.87 ± 0.81 (4.75 ± 2.62) mm
	[71]	3-D TRUS 3-D MRI	Non-linear	1) Modality independent neighborhood descriptor 2) Duality-based convex optimization algorithm	20	TRE DSC MAD MAXD	1.93 ± 0.73 (3.37 ± 1.23) mm 85.7 ± 4.7 (n/a) % 1.84 ± 0.52 (n/a) mm 6.90 ± 2.07 (n/a) mm
	[73]	2-D TRUS 3-D TRUS	Linear	1) Optimize NCC using Powell's method 2) Golden section search technique	14	TRE	1.40 ± 1.18 (3.41 ± 3.26) mm
Shape	[74]	2-D TRUS 2-D MRI	Non-linear	1) Point correspondences obtained from a statistical measure of shape-contexts 2) The radial-basis function of thin-plate splines	20	TRE DSC 95HD	1.60 ± 1.17 (n/a) mm 98.0 ± 0.4 (n/a) % 1.63 ± 0.48 (n/a) mm
	[80]	3-D TRUS 3-D MRI	Non-linear	1) Statistical motion model 2) Expectation maximization algorithm for model-to-image registration	8	TRE	2.40 (8.13) mm
	[75]	3-D TRUS 3-D MRI	Non-linear	1) Coherent point drift algorithm 2) Thin-plate splines	13	TRE	2.00 (2.60) mm
	[81]	3-D TRUS 3-D MRI	Non-linear	1) Statistical motion model 2) Kernel regression analysis	44	TRE	2.40 (6.19) mm
	[82]	3-D TRUS 3-D MRI	Non-linear	1) Finite element model with biomechanical constraint 2) Gaussian mixture model	19	TRE	2.72 ± 1.15 (4.01 ± 1.45) mm
	[83]	3-D TRUS 3-D MRI	Non-linear	1) Statistical shape model 2) Finite element model	19	TRE	2.35 ± 0.81 (4.01 ± 1.45) mm
	[84]	3-D TRUS 3-D MRI	Non-linear	1) Personalized statistical deformable model 2) Hybrid point matching	18	TRE	1.44 ± 0.38 (6.78 ± 1.52) mm
	[85]	3-D TRUS 3-D MRI	Non-linear	1) Robust projective dictionary learning 2) Personalized statistical deformable model	18	TRE	1.51 ± 0.71 (6.78 ± 1.52) mm
	[77]	2.5-D TRUS 3-D MRI	Non-linear	1) Linear stress-strain quasi-static FEM 2) 2.5-D–3-D non-rigid registration	11	TRE	0.72 ± 0.45 (4.62 ± 3.38) mm

DSC, dice similarity coefficient; HD, Hausdorff distance; MAD, mean absolute distance; MAXD, maximum distance; MRI, magnetic resonance imaging; TRE, target registration error; TRUS, transrectal ultrasound.

for MRI-TRUS registration. They also developed a duality-based convex optimization algorithm to compute modality-independent neighborhood descriptor similarity. De Silva et al. [72] used Powell's method to optimize the normalized cross-correlation metric between images, completing the linear registration of 2-D TRUS to 3-D TRUS. Later, Gillies et al. [73] also used Powell's method to optimize the normalized cross-correlation metric and realized real-time registration of 2-D and 3-D TRUS.

Shape-based methods. It remains challenging to use intensity-based metrics to evaluate the similarity of multi-modality images. Therefore, most of MRI-TRUS and CT-TRUS registration approaches sought the shape-based similarities as the solution. Although the shape-based methods required additional steps to obtain the prostate region or

corresponding landmarks, they offered more reliable and robust registration for multi-modality tasks. Mitra et al. [74] introduced a non-linear thin-plate spline regularized 2-D MRI-TRUS registration method. The boundary point correspondences were estimated based on a statistical measure of shape-contexts. Zetting et al. [75] applied the coherent point drift (CPD) algorithm to elastically align surfaces extracted from TRUS and MRI. They then propagated the surface deformation to the whole gland using the thin-plate spline interpolation. Lee et al. [76] proposed a deformable CT-TRUS registration method based on the structural descriptor map, calculated by solving the Laplace's equation using the segmented prostate surface. The structural descriptor map represented the surface distribution and could be used for deformable

registration. Samei et al. [77] proposed an efficient algorithm to extract arbitrary slices in real-time from deformed 3-D images represented by a discrete grid. They simulated tissue deformation using a patient-specific finite element model (FEM) with boundary conditions for image-guided, robot-assisted laparoscopic radical prostatectomy. Later, Samei et al. [78] incorporated this technology into a virtual reality-based robot-assisted laparoscopic radical prostatectomy system.

Certain methods [79,80] used both statistical shape modeling (SSM) and biomechanical modeling to capture the motion of the prostate, which has been proved as a robust solution for MRI-TRUS registration. Leveraging the SSM and biomechanical modeling, Hu et al. [80] further calculated the normal vector field of the prostate surface in TRUS and used the expectation maximization algorithm to maximize the log-likelihood function for model-to-image registration. Hu et al. [81] later used kernel regression analysis to express the multivariate subject-specific probability density function for the construction of subject-specific statistical motion model. Khallaghi et al. [82] used a probabilistic framework based on Gaussian mixture model to combine FEM with biomechanical prior knowledge for extrapolating and constraining deformation fields during MRI-TRUS registration. Khallaghi et al. [83] used probabilistic SSM-FEM to map two surfaces and their interiors to a common intermediate SSM instance, aligning MRI to 3-D TRUS through this intermediate shape. Wang et al. [84] introduced a hybrid point matching method to establish reliable surface point correspondences. A series of FEM were conducted using personalized anatomical and biomedical information. And a personalized statistical deformable model was constructed by the principal component analysis of FEMs to estimate the deformation. To enhance the efficacy of SSM in [84,85] developed a robust projective dictionary learning algorithm to integrate dimensionality reduction and dictionary learning into a unified shape prior modeling framework, and applied it for MRI-TRUS registration.

DL methods. With the rapid development of GPUs, using DL methods to solve non-linear registration with high computational complexity has become mainstream. These DL methods for TRUS image registration can be categorized into image-based networks, label-driven networks and point set networks. The first two types often take images as input, while the last one uses surface point clouds. Image-based networks mainly rely on the similarity between moving and fixed images as the loss function to update network parameters. In contrast, label-driven networks directly use prostate annotations or landmarks to aid registration, either by incorporating them into the loss function or by directly registering them. Point set networks transform the image registration problem in the form of point cloud matching and train the network using the point-based loss function. Table 10 introduces the representative methods in each category.

Image-based network. Some methods have focused on the development of novel network architectures. Yan et al. [86] proposed an adversarial MRI-TRUS registration framework, which trained two CNNs concurrently—a generator for image registration and a discriminator to assess the registration quality. This method only considered linear transformation and required ground-truth transformation for the supervised learning. Guo et al. [87] proposed a 2-D–3-D TRUS registration network. This network used a dual-branch encoding module to extract 2-D and 3-D features for the estimation of linear transformation parameters. And a 2-D plane sampling module was designed to enable efficient training and inference. This approach was subsequently extended to [88], by newly designing a frame-to-slice correction network to refine the transformation estimation and a similarity filtering mechanism to assess the registration quality. Song et al. [89] introduced a cross-modal attention module to explicitly use spatial correspondence for a linear transformation in 3-D MRI-TRUS registration, and further extended this approach to other applications [90]. Sang et al. [91] divided their model into three stages, each of which split and merged fixed and moving images, then fed them into an encoder based on Swin Transformer [66] to obtain an affine transformation for MRI-TRUS.

Other methods have explored various training strategies and loss functions. Haskins et al. [92] used a CNN to learn similarity metrics for the representation of MRI-TRUS, and then used the learned similarity metric to optimize the registration. Guo et al. [93] used data generation methods to create diverse training data distributions, allowing the network to perform well for MRI-TRUS registration. Song et al. [94] introduced the transformed grid distance loss, which addressed the issue of rotation representation and bridged the gap between translation and rotation. Combining 3-D diffusion models [95] and GANs, Ma et al. [96] translated MRI and US images into an intermediate pseudo-modality, preserving details while generating more similar textures for registration. However, this study did not report the accuracy of the registration.

Label-driven network. These networks leveraged prostate annotations or landmarks to evaluate the similarity of multi-modality prostate images. Hu et al. [97] optimized a discriminator network to identify the deformation field predicted by registration network from FE-simulated motion data. The MRI-TRUS registration network simultaneously aimed to maximize similarity between anatomical labels to drive image alignment and minimize an adversarial generator loss that measured divergence between the predicted and simulated deformation. Hu et al. [98] also investigated using various types of identifiable corresponding anatomical structures to train the network for the prediction of dense voxel correspondence. These anatomical structures could be prostate region, vessels, point landmarks or other ad hoc structures. Later, Hu et al. [99] extended their work [98] by designing a new multiscale Dice for the network training and an improved memory-efficient network architecture. Hu et al. [100] applied segmentation concepts to registration, predicting the transformed region of interest directly without predicting the deformation field. Zeng et al. [101] used a CNN for segmentation and then supervised the training of registration network using a surface loss. Chen et al. [102] also used segmentation-based learning to train the MRI-TRUS registration network for the application of prostate brachytherapy. Song et al. [103] trained a CNN to extract landmarks and then leveraged these landmarks for affine registration. Azampour et al. [104] registered MRI to TRUS images via deformable registration, translating MRI into the ultrasound domain while preserving structural content using contrastive unpaired translation.

Point set network. Baum et al. [105] described a point set registration algorithm based on a free point transformer network for points extracted from segmented MRI-TRUS surfaces. Based on the preliminary work [105,106], they developed a partial point-set registration network, which allowed non-linear matching without known correspondence or heuristic constraints. Fu et al. [107] used tetrahedron meshing to generate volumetric prostate point clouds from segmented masks and trained a point cloud matching network using deformation fields generated by FE analysis. Min et al. [108] developed a physically-informed neural network to impose elastic constraints on the estimated displacements and formulated an end-to-end registration network training algorithm by minimizing surface distances as estimated boundary conditions in partial differential equations.

PCa classification and detection

Modalities

As depicted in Table 11, the predominant modalities for TRUS-based PCa classification and detection methods are B-mode TRUS, as well as CEUS and micro-US. With the advent of multi-modality imaging techniques, such as SWE, there has been a growing interest in multi-modality TRUS-based PCa diagnosis in recent years.

Classification and detection methods

We categorize the TRUS-based PCa diagnosis methods into two classes: traditional methods and DL methods. Some representative studies are summarized in Table 12.

Table 10
Overview of deep Learning methods for prostate TRUS registration

Deep Learning Methods	References	Dimensions Modalities	Deformation	Methods	Samples	Results	
						Metrics	Values: final (initial)
Image-based Network	[86]	3-D TRUS	Linear	1) Adversarial learning 2) Supervised-learning using ground truth	763	TRE	3.48 (6.11) mm
	[92]	3-D TRUS	Linear	1) Use CNNs to learn similarity metrics for MRITRUS 2) Composite optimization strategy	679	TRE	3.86 (16) mm
	[93]	3-D TRUS	Linear	1) Coarse-to-fine multi-stage framework 2) Generate different training data distributions	679	TRE	3.57 ± 2.03 (8) mm
	[89]	3-D TRUS	Linear	1) Cross-modal attention mechanism	662	TRE	3.63 ± 1.86 (8) mm
	[87]	3-D TRUS	Linear	1) Dual-branch feature extraction module 2) Differentiable 2-D slice sampling module	619	TRE	2.73 (5.86) mm
	[88]	3-D TRUS	Linear	1) Frame-to-slice correction network 2) Similarity filtering mechanism	618	TRE	6.95 ± 8.03 (n/a) mm
Label-driven Network	[97]	3-D TRUS	Non-linear	1) Weakly-supervised anatomical-label-driven network 2) Adversarial deformation regularization	108	TRE DSC	6.3 (n/a) mm 82 (n/a) %
	[98]	3-D TRUS	Non-linear	1) Label-driven weakly-supervised learning	111	TRE DSC	4.2 (n/a) mm 88 (n/a) %
	[99]	3-D TRUS	Non-linear	1) Multiscale Dice for weakly-supervised training 2) Memory-efficient network architecture	108	TRE DSC	3.6 (n/a) mm 87 (n/a) %
	[100]	3-D TRUS	Non-linear	1) Conditional image segmentation paradigm	115	TRE DSC	2.1 (n/a) mm 92 (n/a) %
	[104]	3-D TRUS	Non-linear	1) Image translation and segmentation	708	TRE DSC 95HD	3.58 ± 1.44 (n/a) mm 89.2 ± 3.86 (n/a) % 1.81 ± 0.61 (n/a) mm
		3-D MRI					4.7 ± 1.8 (5.1 ± 1.7)
Point Set Network	[105]	3-DTRUS	Non-linear	1) Free point transformer network	108	TRE HD	6.3 ± 1.6 (10.7 ± 2.6)
	[106]	3-D TRUS	Non-linear	1) Data-driven learning without heuristic 2) Variable number of points in training and inference	108	TRE HD	4.75 ± 1.45 (5.1 ± 1.7) 6.18 ± 1.36 (10.7 ± 2.6)
	[107]	3-D TRUS	Non-linear	1) Biomechanical constraints via finite element analysis 2) Surface Chamber distance loss	50	TRE DSC HD	1.57 ± 0.77 (n/a) mm 94 ± 2 (n/a) % 2.96 ± 1.00 (n/a) mm
	[108]	3-D TRUS	Non-linear	1) Biomechanical constraints exerted from soft-tissue-modeling partial differential	77	TRE	1.90 ± 0.52 (n/a) mm

CCN, convolutional neural network; DSC, dice similarity coefficient; HD, Hausdorff distance; MRI, magnetic resonance imaging; TRE, target registration error; TRUS, transrectal ultrasound.

Traditional methods. These methods have paid attention to analyzing the hand-crafted features extracted from images to conduct diagnosis. Mohamed et al. [109] extracted texture features from TRUS, including the gray-level dependence matrix and gray-level difference vector. These features were then ranked and selected using a mutual information-based selection algorithm to ensure that only relevant features were

used for classification using SVMs. Han et al. [110] presented a method that combined multi-resolution auto-correlation texture features with clinical features, such as tumor location and shape, using an SVM for classification. Moradi et al. [111] searched for the best-performing feature subsets from texture features, radiofrequency time series features, and Lizzi–Feleppa features, and combined these optimal subsets to

Table 11
Prostate cancer classification studies categorized as using single modality and multimodality

	Classifications	References
Single modality	B-mode TRUS	[109–113,116,123,127,241–253]
	CEUS	[117,118,120,254–257]
	Micro-US	[119,121,122,124]
Multimodality	TRUS + CEUS	[115]
	TRUS + SWE	[125,126]
	TRUS + SWE + CEUS	[114,258]

CEUS, contrast-enhanced ultrasound; SWE, shear wave elastography; TRUS, transrectal ultrasound; US, ultrasound.

construct an SVM classifier. Maggio et al. [112] designed a multi-feature kernel classification model based on generalized discriminant analysis. They further used the predictive deconvolution to reduce system-dependent effects. Glotsos et al. [113] developed a multi-classifier system for discriminating between normal, infectious, and cancerous prostate based on the texture analysis of TRUS. A two-level hierarchical decision tree was designed to first distinguish between normal and abnormal cases and then to further classify the abnormal cases into infectious and cancerous categories. Classification at each level was conducted using three classifiers—cubic least square mapping probabilistic neural network, quadratic Bayesian, and SVM. Wildeboer et al. [114] constructed a classification model that used TRUS, SWE and CEUS. Initially, features concerning contrast perfusion and dispersion were extracted from CEUS videos. Subsequently, radiomics features were collected from all imaging modalities, and a random forest model was used for classification. Sun et al. [115] collected clinical risk factors, including age, PSA density, serum total PSA, rise time, as well as radiomics features from target lesions identified in B-mode and CEUS examination. These features were then used to develop a risk factors–radiomics combined model through multivariable logistic regression analysis.

DL methods. The DL methods for TRUS-based PCa diagnosis were primarily aimed at achieving a more powerful feature representation that enhanced the classification performance. Shi et al. [116] used a deep polynomial network to improve the representation performance of the initially extracted texture features for small TRUS dataset, and further proposed a stacked deep polynomial network algorithm to enhance the original deep polynomial network. Azizi et al. [117] used deep belief

networks to automatically learn high-level features from CEUS data for PCa detection and grading. Additionally, they used GMMs to model the distribution of these features across different Gleason grades. Feng et al. [118] proposed a 3-D CNN to extract the spatial-temporal features uniformly from the CEUS videos. The video frames were split into small image tensors, and each tensor was treated as a sample. Shao et al. [119] used a generative adversarial network–based three-player min-max game framework to address data source heterogeneity and enhance classification performance for PCa. A modified U-net was proposed to encode multi-scale PCa-related information, thereby facilitating more effective data analysis and classification. Javadi et al. [120] used multiple instance learning networks to learn from TRUS regions corresponding to biopsy core pathology, which represented a statistical distribution of PCa. Independent conditional variational auto encoders were trained to extract label-invariant features from radiofrequency data, facilitating the generation of synthetic data that enhanced multiple instance learning network training. Gilany et al. [121] proposed a DL model for the detection of PCa using micro-US. They used a co-teaching paradigm to handle label noise and incorporated evidential DL to estimate predictive uncertainty. This combined approach addressed challenges such as weak labels and out-of-distribution data. Gilaney et al. [122] proposed a multi-scale and context-aware DL method for PCa detection from micro-US. Self-supervised learning was used to train a CNN for extracting features from ROIs, while a Transformer model with attention mechanisms was used for feature aggregation. Sun et al. [123] proposed a mask-guided hierarchical 3-D CNN for identifying clinically significant PCa from TRUS videos. Wilson et al. [124] used a self-supervised learning approach to leverage abundant unlabeled micro-US data to train the PCa detection model. By pretraining models with self-supervised learning and fine-tuning them on limited labeled data, the approach outperformed traditional supervised learning methods. Wu et al. [125] proposed a framework for the classification of clinically significant PCa from multi-modality TRUS videos. The framework used two encoders to extract features from B-mode and SWE. An adaptive spatial fusion module was introduced to aggregate two modalities’ features. An orthogonal regularized loss was further used to mitigate feature redundancy. Wu et al. [126] further designed a hybrid attention module to aggregate features from B-mode and SWE, then used a prototype correction module to refine these features for better classification of clinically significant PCa from multi-modality TRUS videos. Choi et al. [127] learned ultrasound biomarkers by leveraging non-registered multimodal image correlations (ultrasound, MRI, histopathology), feeding enriched features into a 3-D–UNet for PCa detection.

Table 12
Overview of TRUS-based prostate cancer classification and detection methods

Types	References	Methods	Samples	Results			
				Accuracy (%)	Sensitivity (%)	Specificity (%)	AUC (%)
Traditional methods	[109]	Texture features, SVM	33	87.75	83.33	90.00	-
	[110]	Texture features, clinical features, SVM	51	96.40	92.00	95.90	-
	[111]	Texture features, radiofrequency features, SVM	35	-	-	-	95.00
	[112]	Multi-feature kernel classification, predictive deconvolution	37	89.00	79.00	89.00	93.00
	[113]	Texture features, multi-classifier system, hierarchical decision tree	165	88.70	86.70	89.80	-
	[114]	Contrast-enhanced features, radiomics features, random forest	50	-	-	-	75.00
	[115]	Clinical risk factors, radiomics, multivariable logistic regression	166	82.00	80.00	83.00	89.00
	[116]	Stacked deep polynomial network, representation learning	70	86.11	76.40	91.45	-
Deep learning methods	[117]	Deep belief network, tissue mimicking, Gaussian mixture model	197	68.00	63.00	67.00	72.00
	[118]	3-D convolutional neural network, spatial-temporal features	27841	90.18	82.83	91.45	-
	[119]	Generative adversarial network, modified U-net	6607	-	95.10	87.70	93.40
	[120]	Multiple instance learning, conditional variational auto encoders	339	66.00	77.00	55.00	68.00
	[121]	Co-teaching paradigm, evidential deep learning	472	-	67.38	88.20	87.76
	[122]	Transformer, CNN, SSL	1398	-	88.00	51.00	80.00
	[123]	3-D CNN, prostate segmentation	832	-	81.00	78.00	85.00
	[124]	SSL, pretrain and fine-tune	1028	-	-	-	90.99
	[125]	3-D CNN, adaptive spatial fusion module, orthogonal regularization	512	79.00	-	-	84.00
	[126]	3-D CNN, hybrid attention module, prototype correction module	512	81.00	86.00	73.00	86.00

AUC, area under the receiver operating characteristic curve; SVM, support vector machine; SSL, self-supervised learning; TRUS, transrectal ultrasound.

Table 13

Needle detection approaches categorized as applications in biopsy and brachytherapy

Application Scenarios	References
Biopsy	[130,259–263]
Brachytherapy	[128,129,131–136,264–274]

Needle detection

Biopsy and brachytherapy

As shown in Table 13, most detection and segmentation approaches for interventional needles from TRUS have been focused on the clinical scenarios of biopsy and brachytherapy procedures. In the biopsy, needles are inserted to obtain targeted tissue samples, which are analyzed to identify and diagnose PCa. In the brachytherapy, needles are used to implant radioactive seeds directly into cancerous tissues, maximizing treatment efficacy while minimizing damage to healthy areas.

Needle detection methods

We categorize these methods into traditional methods and DL methods. Some representative studies are given in Table 14.

Traditional methods. Wei et al. [128] used gray-level change detection by comparing 3-D TRUS captured before and after needle insertion. The needle was segmented from the difference map using a series of steps including thresholding, removal of spurious signals, and linear regression. Waite et al. [129] used random sample consensus to reconstruct the 3-D needle shape during TRUS-guided prostate brachytherapy. The Hough transform, traditionally used in image processing for the identification of geometrical shapes like lines and circles, has been adapted for the segmentation of interventional needles in TRUS. Cool et al. [130] introduced a temporal-based algorithm that harnessed the Hough transform to detect and track needle edges across multiple 2-D TRUS frames. Qiu et al. [131] further used the 3-D Hough transform, leveraging edge detection techniques in conjunction with assembly into coherent structures. This method facilitated the estimation of needle deflection angles with enhanced precision. Qiu et al. [132] grouped voxel gradient vectors into line support regions. Each line support region was processed using least-squares fitting and a 3-D randomized Hough transform to estimate the needle axis.

DL methods. In recent years, as DL has rapidly advanced, it has also gained increasing prominence in the task of needle detection. Wang et al. [133] developed a modified U-net for segmenting pixels belonging to brachytherapy needles from TRUS, supplemented by an additional VGG-16-based network that predicted the locations of the needle tips. Zhang et al. [134] adopted a weakly supervised framework that referenced corresponding CT images owing to their higher signal-to-noise ratio. The

approach was centered around the bidirectional convolutional sparse coding model, which concurrently learned dictionaries for both US and CT images to enhance needle visualization and reduce noise. The whole process included image preprocessing, needle reconstruction using the bidirectional convolutional sparse coding model, and needle modeling through iterative random sample consensus algorithms. Zhang et al. [135] used a large margin mask R-CNN model to localize needle shafts in TRUS, and further used a needle-based density-based spatial clustering of applications with noise algorithm to refine shaft localization and detect needle tips. Zhang et al. [136] integrated sparse dictionary learning with order-graph regularization to enhance spatial continuity in TRUS. The key idea lied in a label-free approach that leveraged auxiliary images without needles to learn intrinsic features for reconstructing target images.

Discussion and future research directions

In this section, we discuss the current challenges and suggest possible research directions for each of the main tasks in TRUS image processing.

Prostate gland segmentation

The evolution of TRUS segmentation techniques is pivotal for enhancing the efficiency of PCA diagnosis and treatment. The intrinsic challenge in TRUS segmentation arises from its imaging characteristics and the physiological properties of the prostate, which collectively make the delineation of prostate boundaries in TRUS ambiguously. The Prostate Gland Segmentation section provides a narrative review of the research progress in the field of TRUS segmentation, analyzing it from the perspectives of imaging modalities, dimensions, and segmentation methods. Diverse imaging modalities such as B-mode, elastography, and micro-US imaging offer various structural representations, aiding in the identification of the prostate's morphology and boundaries. Moreover, 2-D, 2.5-D, and 3-D segmentation methods each have their advantages, ranging from efficient segmentation of single slices to comprehensive analysis of the entire volume, offering a variety of technical options for accurate prostate segmentation. Traditional segmentation methods and DL-based approaches each have their characteristics, with DL showing great potential in improving segmentation accuracy.

According to Table 3, for traditional 2-D TRUS gland segmentation methods, prostate segmentation based on principal curves achieves excellent results (DSC of >95%), although it is semi-automatic. Among fully automatic 2-D segmentation methods, ASM-based approaches also yield satisfactory results. In 3-D segmentation, methods leveraging symmetry and convex optimization demonstrate high accuracy (DSC of >93%). For DL methods according to Table 4, 2-D segmentation using multi-scale strategies achieves high DSC values, whereas for 3-D segmentation, current DL methods generally underperform compared to traditional methods. However, some approaches, such as Xu et al. [54] and Wang et al. [61], achieve promising results.

Table 14

Overview of methods on needle detection from TRUS

References	Methods	Samples	Results		
			Shaft Error (mm)	Shaft Error (°)	Tip Error (mm)
[128]	Gray-level change detection, thresholding, linear regression	Phantom	-	0.52 ± 0.16	0.82 ± 0.11
[130]	Hough transform, temporal information	108	-	2.30 ± 2.00	2.10 ± 4.00
[131]	3-D Hough transform	35	-	0.80 ± 0.21	0.90 ± 0.32
[132]	3-D phase grouping technique, 3-D Hough transform	50	-	0.95 ± 0.15	1.15 ± 0.15
[129]	RANSAC	Phantom	0.37 ± 0.15	-	-
[134]	Bidirectional convolutional sparse coding, RANSAC	10	0.11 ± 0.09	-	0.32 ± 0.35
[135]	Large margin mask R-CNN	23	0.09 ± 0.04	-	0.32 ± 0.30
[136]	Unsupervised order-graph regularized sparse dictionary learning	91	0.19 ± 0.13	-	1.01 ± 1.74

RANSAC, random sample consensus; R-CNN, regions with convolutional neural network (CNN) features; TRUS, transrectal ultrasound.

Despite significant advancements in TRUS segmentation techniques, multiple challenges remain. The ambiguity and noise in TRUS images pose a particular difficulty for the automatic segmentation of prostate boundaries. Moreover, although 3-D segmentation methods offer more comprehensive structural information of the prostate, their high computational costs and demands on computational resources limit their application in clinical practice. The scarcity and inconsistency of data quality also challenge the generalizability of models, especially in surgical navigation and treatment planning, where high-precision segmentation is required. The demand for real-time performance further complicates the design of segmentation algorithms, particularly in surgical environments where there are stringent requirements for the response speed of the algorithms.

Future research should focus on enhancing the automation, accuracy, and real-time performance of TRUS segmentation techniques. Automated and intelligent algorithms will reduce user interaction, enhancing the efficiency and repeatability of segmentation. Continuous optimization of DL models, including improvements in network architecture and training strategies, will better adapt to the specific requirements of prostate segmentation. Fewshot learning, semi-supervised and weakly supervised learning methods will address the scarcity of high-quality annotated data, improving model performance with limited data. Moreover, cross-modality and multi-task learning methods will use the correlation between different imaging modalities and related clinical tasks to enhance the overall effectiveness of segmentation. Finally, improving the interpretability and generalizability of models, as well as optimizing models to meet the demands of real-time processing, will be key to advancing the development of prostate segmentation technology.

Prostate image registration

In the domain of PCa diagnosis and therapy, the registration of TRUS images constitutes a critical technological component. By aligning preoperative imaging (could be 3-D MRI, CT or TRUS) with real-time 2-D TRUS obtained during surgery, it facilitates the precise targeting and treatment by clinicians. We take MRI–TRUS registration for instance. The prerequisite for this process is the acquisition of MRI, typically T2-weighted multiparametric MRI. Diagnosis is performed on the MRI to identify biopsy locations. During intraoperative MRI–TRUS fusion, there are currently two main approaches: (1) Cognitive fusion: this method involves the ultrasound operator observing both TRUS and MRI simultaneously to locate the suspicious regions identified on the MRI within the TRUS images. Although this approach is operator friendly, it requires a deep understanding of both modalities and the ability to find corresponding locations between them, necessitating an experienced operator. (2) Image registration-based fusion: This technique uses algorithms to perform rigid or deformable registration of the prostate gland between MRI and TRUS images, often involving segmentation of the gland in both modalities. The registered spatial correspondence is then used to transfer the biopsy target location from the MRI to the TRUS image. This method significantly decreases the reliance on operator experience in image interpretation but requires additional computational resources for running registration and segmentation algorithms, and it must account for potential algorithmic errors. Conventional image registration approaches mainly include intensity-based methods and shape-based methods, where the shape-based statistical model combined with biomechanical modeling methods provides a robust set of solutions. Advancing with the evolution of DL, registration methods driven by point clouds or annotated labels have exhibited enhanced automation and precision by discerning intricate mappings between sets of images.

Tables 9 and 10 show that, from a performance perspective, traditional methods generally outperform DL methods in terms of registration accuracy (with lower TRE). It is possible that some iterative strategies used in traditional methods could be integrated into current DL

approaches to achieve better results, balancing accuracy and real-time performance. Interestingly, the best-performing methods in both traditional and DL categories (Samei et al. [77], Min et al. [108]) use FEM, which shows strong research potential by integrating biomechanical modeling to produce more realistic deformations. Additionally, intensity-based traditional methods, such as those of Baumann et al. [70], also achieve favorable results, and their strategies could be incorporated into future DL methods.

Regarding registration modalities and types, traditional methods cover a broader range. In DL approaches, linear registration focuses primarily on 3-D TRUS–MRI registration and 2-D TRUS to 3-D TRUS registration. For non-linear registration, most current DL methods address 3-D multi-modality registration, often requiring additional segmentation to assist in training, including label-driven and point-set methods. In the future, DL research could expand to broader areas, such as deformable 2-D to 3-D TRUS registration, rigid 2-D TRUS to 3-D MRI registration, and deformable 2-D TRUS to 3-D MRI registration. Although Ma et al. [96] use an unsupervised 3-D generation method to generate fake modality for further registration, it does not provide additional details on the registration approach or results. However, this direction is quite innovative.

According to Tables 9 and 10, only traditional methods have explored rigid registration from 2-D TRUS to 3-D MRI, but these methods require iterative processes. In contrast, current DL approaches are limited to rigid registration from 3-D to 2-D TRUS or deformable registration between 3-D MRI and 3-D TRUS, with the additional requirement of segmentation. Thus, using DL for registration necessitates acquiring 3-D TRUS images from patients or generating 3-D TRUS from 3-D MRI through generative techniques. This process involves segmenting and registering the gland in both 3-D images, then performing rigid registration of 3-D to 2-D TRUS intraoperatively, and finally mapping the 2-D TRUS slices onto the 3-D MRI using deformable registration. This workflow is currently complex, requiring additional computational resources and software, and is not very convenient for clinical use.

Most of the articles we surveyed involve multi-modality registration, predominantly focusing on 3-D–3-D registration. Consequently, shape-based methods or label-driven networks are often used in these tasks. These methods are generally unaffected by different modalities and have demonstrated promising results in preoperative applications. However, shape-based methods, which register according to the prostate contours, tend to produce sparse deformation fields, leading to sub-optimal deformation effects in internal areas. Additionally, both shape-based and label-driven methods require segmentation and annotation, which not only suffer from the segmentation challenges discussed in the Prostate Gland Segmentation section but also increase time complexity, rendering them unsuitable for intraoperative scenarios. Intraoperative registration involves the challenging leap from 3-D to 2-D dimensions, making it difficult to ensure both accuracy and real-time performance simultaneously, which is why an end-to-end method has yet to be developed. Although image-based methods can quickly generate dense deformation fields, their accuracy needs improvement. Finding an effective similarity metric to measure different modalities may be key to solving this problem.

Looking ahead to the future development of TRUS image registration, a suite of innovative research directions is anticipated to propel the advancement of this field. At the forefront, researchers are committed to crafting novel algorithms that integrate detailed internal structural information of the prostate, alongside the design of loss functions capable of surmounting the disparities between various imaging modalities. An ideal solution would be end-to-end registration, although this is challenging to implement. Alternatively, generating TRUS from MRI or using an intermediate modality could avoid the need for 3-D TRUS acquisition. However, this requires precise image conversion and ensures that tissue information, especially related to PCa, is preserved. Additionally, the integration of SWE into the registration process to leverage the biomechanical properties of tissues for improved registration accuracy is an

important avenue for future exploration. Collectively, these research directions aim to foster progress in TRUS image registration, equipping the clinical realm with more accurate diagnostic and therapeutic tools.

PCa classification and detection

In the realm of PCa classification and detection, B-mode TRUS examination has emerged as a predominant imaging modality, complemented by CEUS, MicroUS, and SWE to enhance the accuracy of diagnosis. Traditional methods are primarily relied on texture features or combined with radiofrequency features for analysis through classifiers like SVM. Moreover, radiomic analysis offers a comprehensive feature assessment, extracting a vast array of quantitative features from images. The application of DL has revolutionized PCa classification, with various network structures and training strategies significantly improving classification performance.

According to Table 11, the majority of current methods rely on single-modality input, with only five using multi-modality approaches. Notably, none of the single-modality methods independently consider elastography. From a clinical perspective, elastography and contrast-enhanced imaging provide important indicators for diagnosing PCa, so there is significant room for research in combining multiple modalities in computer-aided PCa diagnosis. Table 12 highlights that, in terms of area under the receiver operating characteristic curve, DL methods have not shown a substantial improvement over traditional methods, despite using larger sample sizes. Among traditional methods, SVM approaches based on texture features perform exceptionally well. Combining the texture features from traditional methods with DL approaches could be a promising direction for future research.

Several challenges persist in this field. Data annotation remains a difficult and time-consuming task owing to the intricate nature of prostate lesions in TRUS. Additionally, the heterogeneity of data sources and the limited availability of high-quality labeled data complicate the development of robust models. These issues underscore the need for innovative solutions to enhance data quality and model performance.

Future research should explore the integration of multi-modality data and advanced learning strategies to overcome these challenges. By combining various imaging modalities and using techniques like weakly supervised and semi-supervised learning, researchers can better use the vast amounts of available but unlabeled data. Such approach can help to mitigate the difficulties in data annotation and improve the generalization capabilities of their models. Furthermore, although most current studies focus on classification tasks, there is a crucial need to develop methods for lesion-scale detection. Advancing research in this direction will enable more precise localization and characterization of cancerous regions, enhancing the overall efficacy of PCa diagnostics in clinical practice.

Needle detection

Recent advancements in interventional needle detection have leveraged both traditional and DL methods. Traditional techniques, such as the Hough transform and random sample consensus algorithms, have been used to detect and track needle edges in TRUS images. These methods rely on identifying geometrical shapes and managing noise and artifacts effectively. Meanwhile, DL approaches have revolutionized needle detection by automatically learning complex patterns from large datasets, improving the accuracy and efficiency of needle detection.

Despite these advancements, several challenges remain in this field. The poor imaging quality of TRUS often complicates the detection process. Furthermore, there is often a discrepancy in annotating the gold standard, leading to errors in needle segmentation. These issues highlight the need for more robust techniques to enhance image quality and reduce annotation errors.

Future research should consider the inherent errors in the gold standard annotations, weakly-supervised and semi-supervised learning

methods should be explored to improve model training. Further advancements could include developing innovative algorithms that can better handle the inherent noise and artifacts in TRUS images, paving the way for more precise and reliable prostate needle segmentation methods. The integration of these techniques into clinical workflows will further facilitate the delivery of personalized and targeted therapies, contributing to the overall improvement in patient care and outcomes.

Summary

This paper conducts a comprehensive review of the advancements in TRUS image processing. The paper meticulously reviews a plethora of studies spanning two decades, delineating the paradigm shift from conventional methods to DL approaches. For the segmentation, the paper summarizes the traditional shape/contour-based, region-based, machine learning methods, as well as the DL models. For 3-D TRUS segmentation, the exigency for high accuracy in preoperative planning, image registration, and volume measurement is paramount, necessitating solutions to low image resolution and large shape variations. Conversely, 2-D TRUS segmentation confronts the challenge of achieving real-time speed, especially in intraoperative navigation scenarios. For the registration, the paper deliberates on the efficacy of traditional intensity-based and shape-based methods, as well as the burgeoning DL approaches, including image-based, label-driven, and point set methods. It notes the predominance of multi-modality 3-D–3-D registration tasks and the challenges associated with real-time property and accuracy in intraoperative settings. For the PCa diagnosis, the paper highlights the advancements made by traditional texture feature analysis and DL's capacity to discern complex patterns from large datasets. It acknowledges the enduring challenges of data annotation and the heterogeneity of data sources, advocating for innovative solutions to enhance data quality and model performance. For the needle detection, traditional geometrical detection methods and DL's automatic pattern recognition have improved accuracy and efficiency. This paper points out the necessity for more robust techniques to address poor imaging quality and reduce annotation errors, suggesting the exploration of weakly supervised and semi-supervised learning methods as future directions. In conclusion, this survey provides an exhaustive overview of the current methodologies and challenges in prostate TRUS image processing and suggests potential research directions to advance the field further.

Conflict of interest

The authors declare no competing interests.

Acknowledgments

The authors would like to thank the editor, the associate editor and the anonymous reviewers for their constructive comments and great efforts to review this survey paper. This work was supported in part by the National Natural Science Foundation of China under Grants 62471306 and 62071305, in part by the Guangdong-Hong Kong Joint Funding for Technology and Innovation (2023A0505010021), in part by the Shenzhen Medical Research Fund under Grant D2402010, and in part by the Guangdong Basic and Applied Basic Research Foundation under Grant 2022A1515011241.

References

- [1] Siegel RL, Miller KD, Wagle NS, Jemal A. Cancer statistics, 2023. *CA Cancer J Clin* 2023;73:17–48.
- [2] Xia C, Dong X, Li H, Cao M, Sun D, He S, et al. Cancer statistics in China and United States, 2022: profiles, trends, and determinants. *Chin Med J* 2022;135:584–90.
- [3] Rawla P. Epidemiology of prostate cancer. *World J Oncol* 2019;10:63.
- [4] Semsarian CR, Ma T, Nickel B, Barratt A, Varma M, Delahunt B, et al. Low-risk prostate lesions: An evidence review to inform discussion on losing the cancer label. *Prostate* 2023;83:498–515.

- [5] Naji L, Randhawa H, Sohani Z, Dennis B, Lautenbach D, Kavanagh O, et al. Digital rectal examination for prostate cancer screening in primary care: a systematic review and meta-analysis. *Ann Fam Med* 2018;16:149–54.
- [6] Lilja H, Ulmert D, Vickers A J. Prostate-specific antigen and prostate cancer: prediction, detection and monitoring. *Nature Reviews Cancer* 2008;8(4):268–78.
- [7] Hricak H, Choyke PL, Eberhardt SC, Leibel SA, Scardino PT. Imaging prostate cancer: a multidisciplinary perspective. *Radiology* 2007;243(1):28–53.
- [8] Borghesi M, Ahmed H, Nam R, Schaeffer E, Schiavina R, Taneja S, et al. Complications after systematic, random, and image-guided prostate biopsy. *Eur Urol* 2017;71:353–65.
- [9] Brown AM, Elbuluk O, Merten F, Sankineni S, Margolis DJ, Wood BJ, et al. Recent advances in image-guided targeted prostate biopsy. *Abdominal Imaging* 2015;40:1788–99.
- [10] Ahmed HU, Bosaily AE-S, Brown LC, Gabe R, Kaplan R, Parmar MK, et al. Diagnostic accuracy of multi-parametric MRI and TRUS biopsy in prostate cancer (PROMIS): a paired validating confirmatory study. *Lancet* 2017;389:815–22.
- [11] Frauscher F, Klausner A, Volgger H, Halpern EJ, Pallwein L, Steiner H, et al. Comparison of contrast enhanced color dopplerD targeted biopsy with conventional systematic biopsy: impact on prostate cancer detection. *J Urol* 2002;167:1648–52.
- [12] Oladimeji AT, Jeje EA, Ojewola RW, Adeyomoye AA, Oboke OS, et al. Predictive value of transrectal ultrasonic doppler and elastographic features in prostate cancer detection in Lagos University Teaching Hospital. *J West Afr Coll Sur* 2024;14:218–24.
- [13] Shen D, Wu G, Suk H-I. Deep learning in medical image analysis. *Annu Rev Biomed Eng* 2017;19:221–48.
- [14] Litjens G, Kooi T, Bejnordi BE, Setio AAA, Ciompi F, et al. A survey on deep learning in medical image analysis. *Med Image Anal* 2017;42:60–88.
- [15] Duncan J, Ayache N. Medical image analysis: progress over two decades and the challenges ahead. *IEEE Trans Pattern Anal Machine Intell* 2000;22:85–106.
- [16] Mahdavi SS, Moradi M, Morris WJ, Goldenberg SL, Salcudean SE. Fusion of ultrasound b-mode and vibro-elastography images for automatic 3-D segmentation of the prostate. *IEEE Trans Med Imag* 2012;31:2073–82.
- [17] Jiang H, Imran M, Muralidharan P, Patel A, Pensa J, Liang M, et al. Microsegnet: a deep learning approach for prostate segmentation on micro-ultrasound images. *Comput Med Imaging Graph* 2024;112:102326.
- [18] Zhang L, Zhou SR, Choi M, Fan RE, Sang S, Sonn GA, et al. Deep learning for prostate and central gland segmentation on micro-ultrasound images. *Medical Imaging 2024: Ultrasonic Imaging and Tomography*, 12932. Bellingham WA: SPIE; 2024. p. 34–8.
- [19] Pathak SD, Haynor D, Kim Y. Edge-guided boundary delineation in prostate ultrasound images. *IEEE Trans Med Imag* 2000;19:1211–9.
- [20] Shen D, Zhan Y, Davatzikos C. Segmentation of prostate boundaries from ultrasound images using statistical shape model. *IEEE Trans Med Imag* 2003;22:539–51.
- [21] Wu P, Liu Y, Li Y, Liu B. Robust prostate segmentation using intrinsic properties of TRUS images. *IEEE Trans Med Imag* 2015;34:1321–35.
- [22] Cootes TF, Taylor CJ, Cooper DH, Graham J. Active shape models-their training and application. *Comput Vis Image Underst* 1995;61:38–59.
- [23] Cosío FA. Automatic initialization of an active shape model of the prostate. *Med Image Anal* 2008;12:469–83.
- [24] Bi H, Jiang Y, Tang H, Yang G, Shu H, Dillenseger J-L. Fast and accurate segmentation method of active shape model with Rayleigh mixture model clustering for prostate ultrasound images. *Comput Methods Programs Biomed* 2020;184:105097.
- [25] Badiei S, Salcudean SE, Varah J, Morris WJ. Prostate segmentation in 2D ultrasound images using image warping and ellipse fitting. *Medical Image Computing and Computer Assisted Intervention*. New York: Springer; 2006. p. 17–24.
- [26] Mahdavi SS, Chng N, Spadinger I, Morris WJ, Salcudean SE. Semi-automatic segmentation for prostate interventions. *Med Image Anal* 2011;15:226–37.
- [27] Yan P, Xu S, Turkbey B, Kruecker J. Adaptively learning local shape statistics for prostate segmentation in ultrasound. *IEEE Trans Biomed Eng* 2010;58:633–41.
- [28] Qiu W, Yuan J, Ukwatta E, Tessier D, Fenster A. Rotational-slice-based prostate segmentation using level set with shape constraint for 3D end-firing TRUS guided biopsy. *Medical Image Computing and Computer Assisted Intervention-MICCAI* 2012. New York: Springer; 2012. p. 537–44.
- [29] Fan S, Voon LK, Sing NW. 3D prostate surface detection from ultrasound images based on level set method. *Medical Image Computing and Computer Assisted Intervention. MICCAI 2002*. New York: Springer; 2002. p. 389–96.
- [30] Yuan J, Qiu W, Ukwatta E, Rajchl M, Tai X-C, Fenster A. Efficient 3D endfiring TRUS prostate segmentation with globally optimized rotational symmetry. In: *Proceedings of the IEEE Conference on Computer Vision and Pattern Recognition*; 2013. p. 2211–8.
- [31] Qiu W, Yuan J, Ukwatta E, Sun Y, Rajchl M, Fenster A. Prostate segmentation: An efficient convex optimization approach with axial symmetry using 3-D TRUS and MR images. *IEEE Trans Med Imag* 2014;33:947–60.
- [32] Qiu W, Rajchl M, Guo F, Sun Y, Ukwatta E, Fenster A, et al. 3D prostate TRUS segmentation using globally optimized volume-preserving prior. *Medical Image Computing and Computer Assisted Intervention-MICCAI* 2014. New York: Springer; 2014. p. 796–803.
- [33] Nouranian S, Mahdavi SS, Spadinger I, Morris WJ, Salcudean SE, Abolmaesumi P. An automatic multi-atlas segmentation of the prostate in transrectal ultrasound images using pairwise atlas shape similarity. *Medical Image Computing and Computer Assisted Intervention-MICCAI* 2013. New York: Springer; 2013. p. 173–80.
- [34] Nouranian S, Mahdavi SS, Spadinger I, Morris WJ, Salcudean SE, Abolmaesumi P. A multi-atlas-based segmentation framework for prostate brachytherapy. *IEEE Trans Med Imag* 2014;34:950–61.
- [35] Ghose S, Oliver A, Mitra J, Martí R, Lladó X, Freixenet J, et al. A supervised learning framework of statistical shape and probability priors for automatic prostate segmentation in ultrasound images. *Med Image Anal* 2013;17:587–600.
- [36] Nouranian S, Ramezani M, Spadinger I, Morris WJ, Salcudean SE, Abolmaesumi P. Learning-based multi-label segmentation of transrectal ultrasound images for prostate brachytherapy. *IEEE Trans Med Imag* 2015;35:921–32.
- [37] Yang X, Rossi PJ, Jani AB, Mao H, Curran WJ, Liu T. 3D transrectal ultrasound (TRUS) prostate segmentation based on optimal feature learning framework. *Medical Imaging 2016: Image Processing*, 9784. Bellingham WA: SPIE; 2016. p. 654–60.
- [38] Peng T, Tang C, Wu Y, Cai J. H-SegMed: a hybrid method for prostate segmentation in TRUS images via improved closed principal curve and improved enhanced machine learning. In *J Computer Vis* 2022;130:1896–919.
- [39] Peng T, Wu Y, Zhao J, Wang C, Wu QJ, Cai J. Organ boundary delineation for automated diagnosis from multi-center using ultrasound images. *Expert Systems Appl* 2024;238:122128.
- [40] Zhan Y, Shen D. Automated segmentation of 3D US prostate images using statistical texture-based matching method. *Medical Image Computing and Computer Assisted Intervention-MICCAI* 2003. New York: Springer; 2003. p. 688–96.
- [41] Zhan Y, Shen D. Deformable segmentation of 3-D ultrasound prostate images using statistical texture matching method. *IEEE Trans Med Imag* 2006;25:256–72.
- [42] Gong L, Pathak SD, Haynor DR, Cho PS, Kim Y. Parametric shape modeling using deformable superellipses for prostate segmentation. *IEEE Trans Med Imag* 2004;23:340–9.
- [43] Tutar IB, Pathak SD, Gong L, Cho PS, Wallner K, Kim Y. Semiautomatic 3-D prostate segmentation from TRUS images using spherical harmonics. *IEEE Trans Med Imag* 2006;25(12):1645–54.
- [44] Yan P, Xu S, Turkbey B, Kruecker J. Discrete deformable model guided by partial active shape model for TRUS image segmentation. *IEEE Trans Biomed Eng* 2010;57:1158–66.
- [45] Garnier C, Bellanger J-J, Wu K, Shu H, Costet N, Mathieu R, et al. Prostate segmentation in HIFU therapy. *IEEE Trans Med Imag* 2010;30:792–803.
- [46] Jaouen V, Bert J, Mountris KA, Boussion N, Schick U, Pradier O, et al. Prostate volume segmentation in TRUS using hybrid edge-Bhattacharyya active surfaces. *IEEE Trans Biomed Eng* 2018;66:920–33.
- [47] Ronneberger O, Fischer P, Brox T. U-net: Convolutional networks for biomedical image segmentation. *Medical Image Computing and Computer Assisted Intervention-MICCAI* 2015. New York: Springer; 2015. p. 234–41.
- [48] Lei Y, Tian S, He X, Wang T, Wang B, Patel P, et al. Ultrasound prostate segmentation based on multidirectional deeply supervised V-net. *Med Phys* 2019;46:3194–206.
- [49] Karimi D, Zeng Q, Mathur P, Avinash A, Mahdavi S, Spadinger I, et al. Accurate and robust deep learning-based segmentation of the prostate clinical target volume in ultrasound images. *Med Image Anal* 2019;57:186–96.
- [50] Karimi D, Salcudean SE. Reducing the Hausdorff distance in medical image segmentation with convolutional neural networks. *IEEE Trans Med Imag* 2019;39:499–513.
- [51] Lei Y, Wang T, Roper J, Jani AB, Patel SA, Curran WJ, et al. Male pelvic multi-organ segmentation on transrectal ultrasound using anchor-free mask CNN. *Med Phys* 2021;48:3055–64.
- [52] Xu X, Sanford T, Turkbey B, Xu S, Wood BJ, Yan P. Polar transform network for prostate ultrasound segmentation with uncertainty estimation. *Med Image Anal* 2022;78:102418.
- [53] Wang W, Pan B, Ai Y, Li G, Fu Y, Liu Y. LightCM-PNet: A lightweight pyramid network for real-time prostate segmentation in transrectal ultrasound. *Pattern Recognit* 2024;156:110776.
- [54] Xu X, Sanford T, Turkbey B, Xu S, Wood BJ, Yan P. Shadow-consistent semi-supervised learning for prostate ultrasound segmentation. *IEEE Trans Med Imag* 2021;41:1331–45.
- [55] Orlando N, Gyackov I, Gillies DJ, Guo F, Romagnoli C, DSouza D, et al. Effect of dataset size, image quality, and image type on deep learning-based automatic prostate segmentation in 3D ultrasound. *Phys Med Biol* 2022;67:074002.
- [56] Li Z, Du W, Shi Y, Li W, Gao C. A bi-directional segmentation method for prostate ultrasound images under semantic constraints. *Sci Rep* 2024;14:11701.
- [57] Yang X, Yu L, Wu L, Wang Y, Ni D, Qin J, et al. Fine-grained recurrent neural networks for automatic prostate segmentation in ultrasound images. In: *Proceedings of the AAAI Conference on Artificial Intelligence*, 31; 2017.
- [58] Anas EMA, Mousavi P, Abolmaesumi P. A deep learning approach for real time prostate segmentation in freehand ultrasound guided biopsy. *Med Image Anal* 2018;48:107–16.
- [59] Vaswani A, Shazeer N, Parmar N, Uszkoreit J, Jones L, Gomez AN, et al. Attention is all you need. *Advances in neural information processing systems*, 30. CA, USA: Long Beach: 31st Conference on Neural Information Processing Systems; 2017.
- [60] Wang Y, Deng Z, Hu X, Zhu L, Yang X, Xu X, et al. Deep attentional features for prostate segmentation in ultrasound. *Medical Image Computing and Computer Assisted Intervention MICCAI* 2018. New York: Springer; 2018. p. 523–30.
- [61] Wang Y, Dou H, Hu X, Zhu L, Yang X, Xu M, et al. Deep attentive features for prostate segmentation in 3D transrectal ultrasound. *IEEE Trans Med Imag* 2019;38:2768–78.
- [62] Gium KB, Lalande A, Hussain R, Crehan G. A deep learning method for real-time intraoperative US image segmentation in prostate brachytherapy. *Int J Comput Assist Radiol Surg* 2020;15:1467–76.
- [63] Vesal S, Gayo I, Bhattacharya I, Natarajan S, Marks LS, Barratt DC, et al. Domain generalization for prostate segmentation in transrectal ultrasound images: A multi-center study. *Med Image Anal* 2022;82:102620.
- [64] Peng T, Wang C, Tang C, Gu Y, Zhao J, Li Q, et al. A multicenter study of ultrasound images using a fully automated segmentation architecture. *Pattern Recognit* 2024;145:109925.
- [65] Chen J, Mei J, Li X, Lu Y, Yu Q, Luo Q, et al. TransUNet: Rethinking the U-Net architecture design for medical image segmentation through the lens of transformers. *Med Image Anal* 2024;97:103280.

- [66] Liu Z, Lin Y, Cao Y, Hu H, Wei Y, Zhang Z, et al. Swin transformer: Hierarchical vision transformer using shifted windows. In: Proceedings of the IEEE/CVF international conference on computer vision; 2021. p. 10012–22.
- [67] Cheng B, Misra I, Schwing AG, Kirillov A, Girdhar R. Maskedattention mask transformer for universal image segmentation. In: Proceedings of the IEEE/CVF conference on computer vision and pattern recognition; 2022. p. 1290–9.
- [68] Xu S, Kruecker J, Guion P, Glossop N, Neeman Z, Choyke P, et al. Closed-loop control in fused MR-TRUS image-guided prostate biopsy. Medical Image Computing and Computer Assisted Intervention-MICCAI 2007. New York: Springer; 2007. p. 128–35.
- [69] Hung N, Baumann M, Long J-A, Trocraz J. A 3-D ultrasound robotic prostate brachytherapy system with prostate motion tracking. IEEE Trans Robot 2012;28:1382–97.
- [70] Baumann M, Mozer P, Daanen V, Trocraz J. Prostate biopsy tracking with deformation estimation. Med Image Anal 2012;16:562–76.
- [71] Sun Y, Yuan J, Qiu W, Rajchl M, Romagnoli C, Fenster A. Three-dimensional non-rigid MR-TRUS registration using dual optimization. IEEE Trans Med Imag 2014;34:1085–95.
- [72] De Silva T, Fenster A, Cool DW, Gardi L, Romagnoli C, Samarabandu J, et al. 2D-3D rigid registration to compensate for prostate motion during 3D TRUS-guided biopsy. Med Phys 2013;40:022904.
- [73] Gillies DJ, Gardi L, De Silva T, Zhao S-R, Fenster A. Real-time registration of 3D to 2D ultrasound images for image-guided prostate biopsy. Med Phys 2017;44:4708–23.
- [74] Mitra J, Kato Z, Marti R, Oliver A, Llado X, Sidibe D, et al. A spline-based non-linear diffeomorphism for multimodal prostate registration. Med Image Anal 2012;16:1259–79.
- [75] Zetting O, Shah A, Hennemersperger C, Eiber M, Kroll C, Kiibler H, et al. Multimodal image-guided prostate fusion biopsy based on automatic deformable registration. Int J Comput Assist Radiol Surg 2015;10:1997–2007.
- [76] Lee J, Song DY. CT-ultrasound deformable registration for PET-determined prostate brachytherapy. Medical Imaging 2018: Image-Guided Procedures, Robotic Interventions, and Modeling, 10576. Bellingham WA: SPIE; 2018. p. 706–12.
- [77] Samei G, Goksel O, Lobo J, Mohareri O, Black P, Rohling R, et al. Real-time FEM-based registration of 3-D to 2.5-D transrectal ultrasound images. IEEE Trans Med Imag 2018;37:1877–86.
- [78] Samei G, Tsang K, Kesck C, Lobo J, Hor S, Mohareri O, et al. A partial augmented reality system with live ultrasound and registered preoperative MRI for guiding robot-assisted radical prostatectomy. Med Image Anal 2020;60:101588.
- [79] Hu Y, Ahmed HU, Allen C, Pendsé D, Sahu M, Emberton M, et al. MR to ultrasound image registration for guiding prostate biopsy and interventions. Medical Image Computing and Computer Assisted Intervention-MICCAI 2009. New York: Springer; 2009. p. 787–94.
- [80] Hu Y, Ahmed HU, Taylor Z, Allen C, Emberton M, Hawkes D, et al. MR to ultrasound registration for image-guided prostate interventions. Med Image Anal 2012;16:687–703.
- [81] Hu Y, Gibson E, Ahmed H U, Moore CM, Emberton M, et al. Population-based prediction of subject-specific prostate deformation for MR-to-ultrasound image registration. Med Image Anal 2015;26:332–44.
- [82] Khallaghi S, Sánchez CA, Rasoulou A, Sun Y, Imani F, Khojasteh A, et al. Biomechanically constrained surface registration: Application to MR-TRUS fusion for prostate interventions. IEEE Trans Med Imag 2015;34:2404–14.
- [83] Khallaghi S, Sánchez CA, Rasoulou A, Nouranian S, Romagnoli C, Abdi H, Chang SD, et al. Statistical biomechanical surface registration: Application to MR-TRUS fusion for prostate interventions. IEEE Trans Med Imag 2015;34:2535–49.
- [84] Wang Y, Cheng J-Z, Ni D, Lin M, Qin J, Luo X, et al. Towards personalized statistical deformable model and hybrid point matching for robust MR-TRUS registration. IEEE Trans Med Imag 2016;35:589–604.
- [85] Wang Y, Zheng Q, Heng PA. Online robust projective dictionary learning: shape modeling for MR-TRUS registration. IEEE Trans Med Imag 2018;37:1067–78.
- [86] Yan P, Xu S, Rastinehad AR, Wood BJ. Adversarial image registration with application for MR and TRUS image fusion. Machine Learning in Medical Imaging: 9th International Workshop, MLMI 2018, Held in Conjunction with MICCAI 2018. New York: Springer; 2018. p. 197–204.
- [87] Guo H, Xu X, Xu S, Wood B J, Yan P. End-to-end ultrasound frame to volume registration. Medical Image Computing and Computer Assisted Intervention-MICCAI 2021. New York: Springer; 2021. p. 56–65.
- [88] Guo H, Xu X, Song X, Xu S, Chao H, Myers J, et al. Ultrasound frame-to-volume registration via deep learning for interventional guidance. IEEE Trans Ultrason Ferroelect Freq Control 2023;70:1016–25.
- [89] Song X, Guo H, Xu X, Chao H, Xu S, Turkbey B, et al. Cross-modal attention for MRI and ultrasound volume registration. Medical Image Computing and Computer Assisted Intervention-MICCAI 2021. New York: Springer; 2021. p. 66–75.
- [90] Song X, Chao H, Xu X, Guo H, Xu S, Turkbey B, et al. Cross-modal attention for multi-modal image registration. Med Image Anal 2022;82:102612.
- [91] Sang S, Jahanandish H, Li X, Vesal S, Bhattacharya I, Zhang L, et al. Swin transformer-based affine registration of MRI and ultrasound images of the prostate. Medical Imaging 2024: Ultrasonic Imaging and Tomography, 12932. Bellingham WA: SPIE; 2024. p. 39–44.
- [92] Haskins G, Kruecker J, Kruger U, Xu S, Pinto PA, Wood BJ, et al. Learning deep similarity metric for 3D MR-TRUS image registration. Int J Comput Assist Radiol Surg 2019;14:417–25.
- [93] Guo H, Kruger M, Xu S, Wood BJ, Yan P. Deep adaptive registration of multi-modal prostate images. Comput Med Imaging Graph 2020;84:101769.
- [94] Song X, Chao H, Xu S, Turkbey B, Wood BJ, Wang G, et al. Transformed grid distance loss for supervised image registration. International Workshop on Biomedical Image Registration. New York: Springer; 2022. p. 177–81.
- [95] Ho J, Jain A, Abbeel P. Denoising diffusion probabilistic models. Adv Neural Inf Process Syst 2020;33:6840–51.
- [96] Ma X, Anantrasirichai N, Bolomytis S, Achim A. PMT: Partial-modality translation based on diffusion models for prostate magnetic resonance and ultrasound image registration. Annual Conference on Medical Image Understanding and Analysis. New York: Springer; 2024. p. 285–97.
- [97] Hu Y, Gibson E, Ghavami N, Bonmati E, Moore CM, Emberton M, et al. Adversarial deformation regularization for training image registration neural networks. Medical Image Computing and Computer Assisted Intervention-MICCAI 2018. New York: Springer; 2018. p. 774–82.
- [98] Hu Y, Modat M, Gibson E, Ghavami N, Bonmati E, Moore CM, et al. Label-driven weakly-supervised learning for multimodal deformable image registration. 2018 IEEE 15th International Symposium on Biomedical Imaging. New York: IEEE; 2018. p. 1070–4.
- [99] Hu Y, Modat M, Gibson E, Li W, Ghavami N, Bonmati E, et al. Weakly-supervised convolutional neural networks for multimodal image registration. Med Image Anal 2018;49:1–13.
- [100] Hu Y, Gibson E, Barratt DC, Emberton M, Noble JA, Vercauteren T. Conditional segmentation in lieu of image registration. Medical Image Computing and Computer Assisted Intervention-MICCAI 2019. New York: Springer; 2019. p. 401–9.
- [101] Zeng Q, Fu Y, Tian Z, Lei Y, Zhang Y, Wang T, et al. Label-driven magnetic resonance imaging (MRI)-transrectal ultrasound (TRUS) registration using weakly supervised learning for MRI-guided prostate radiotherapy. Phys Med Biol 2020;65:135002.
- [102] Chen Y, Xing L, Yu L, Liu W, Pooya Fahimian B, Niedermayr T, et al. MR to ultrasound image registration with segmentation-based learning for HDR prostate brachytherapy. Med Phys 2021;48:3074–83.
- [103] Song X, Xu X, Xu S, Turkbey B, Sanford T, Wood BJ, et al. Distance map supervised landmark localization for MR-TRUS registration. Medical Imaging 2023: Image Processing, 12464. Bellingham WA: SPIE; 2023. p. 708–13.
- [104] Azampour MF, Mach K, Fatemizadeh E, Demiryay B, Westenfelder K, Steiger K, et al. Multitask weakly supervised generative network for MR-USegistration. IEEE Trans Med Imag 2024;2 PP.
- [105] Baum ZM, Hu Y, Barratt D C. Multimodality biomedical image registration using free point transformer networks. Medical Ultrasound, and Preterm, Perinatal and Paediatric Image Analysis: First International Workshop, ASUM 2020, and 5th International Workshop, PIPPI 2020, Held in Conjunction with MICCAI 2020. New York: Springer; 2020. p. 116–25.
- [106] Baum ZM, Hu Y, Barratt DC. Real-time multimodal image registration with partial intraoperative point-set data. Med Image Anal 2021;74:102231.
- [107] Fu Y, Lei Y, Wang T, Patel P, Jani AB, Mao H, et al. Biomechanically constrained non-rigid MR-TRUS prostate registration using deep learning based 3D point cloud matching. Med Image Anal 2021;67:101845.
- [108] Min Z, Baum ZM, Saeed SU, Emberton M, Barratt DC, Taylor ZA, et al. Non-rigid medical image registration using physics-informed neural networks. International Conference on Information Processing in Medical Imaging. New York: Springer; 2023. p. 601–13.
- [109] Mohamed SS, Salama MM. Computer-aided diagnosis for prostate cancer using support vector machine. Medical Imaging 2005: Visualization, Image-Guided Procedures, and Display, 5744. Bellingham WA: SPIE; 2005. p. 898–906.
- [110] Han SM, Lee HJ, Choi JY. Computer-aided prostate cancer detection using texture features and clinical features in ultrasound image. J Digit Imaging 2008;21:121–33.
- [111] Moradi M, Abolmaesumi P, Siemens DR, Sauerbrei EE, Boag AH, Mousavi P. Augmenting detection of prostate cancer in transrectal ultrasound images using SVM and RF time series. IEEE Trans Biomed Eng 2008;56:2214–24.
- [112] Maggio S, Palladini A, De Marchi L, Alessandrini M, Speciale N, Masetti G. Predictive deconvolution and hybrid feature selection for computer-aided detection of prostate cancer. IEEE Trans Med Imag 2009;29:455–64.
- [113] Glosos D, Kalatzis I, Theocharakis P, Georgiadis P, Daskalakis A, Ninos K, et al. A multi-classifier system for the characterization of normal, infectious, and cancerous prostate tissues employing transrectal ultrasound images. Comput Methods Programs Biomed 2010;97:53–61.
- [114] Wildeboer RR, Mannaerts CK, van Sloun RJ, Budaus L, Tilki D, Wijkstra H, et al. Automated multiparametric localization of prostate cancer based on B-mode, shear-wave elastography, and contrast-enhanced ultrasound radiomics. Eur Radiol 2020;30:806–15.
- [115] Sun Y, Fang J, Shi Y, Li H, Wang J, Xu J, et al. Machine learning based on radiomics features combining B-mode transrectal ultrasound and contrast-enhanced ultrasound to improve peripheral zone prostate cancer detection. Abdom Radiol 2024;49:141–50.
- [116] Shi J, Zhou S, Liu X, Zhang Q, Lu M, Wang T. Stacked deep polynomial network based representation learning for tumor classification with small ultrasound image dataset. Neurocomputing 2016;194:87–94.
- [117] Aziz S, Bayat S, Yan P, Tahmasebi A, Nir G, Kwak JT, et al. Detection and grading of prostate cancer using temporal enhanced ultrasound: Combining deep neural networks and tissue mimicking simulations. Int J Comput Assist Radiol Surg 2017;12:1293–305.
- [118] Feng Y, Yang F, Zhou X, Guo Y, Tang F, Ren F, et al. A deep learning approach for targeted contrast-enhanced ultrasound based prostate cancer detection. IEEE/ACM Trans Comput Biol Bioinform 2018;16:1794–801.
- [119] Shao Y, Wang J, Wodlinger B, Salcudean SE. Improving prostate cancer (PCa) classification performance by using three-player minimax game to reduce data source heterogeneity. IEEE Trans Med Imag 2020;39:3148–58.
- [120] Javadi G, Samadi S, Bayat S, Pesteie M, Jafari MH, Sojoudi S, et al. Multiple instance learning combined with label invariant synthetic data for guiding systematic prostate biopsy: A feasibility study. Int J Comput Assist Radiol Surg 2020;15:1023–31.

- [121] Gilany M, Wilson P, Jamzad A, Fooladgar F, To MNN, Wodlinger B, et al. Towards confident detection of prostate cancer using high resolution micro-ultrasound. *Medical Image Computing and Computer Assisted Intervention*. New York: Springer; 2022. p. 411–20.
- [122] Gilany M, Wilson P, Perera-Ortega A, Jamzad A, To MNN, Fooladgar F, et al. TRUSformer: Improving prostate cancer detection from micro-ultrasound using attention and self-supervision. *Int J Comput Assist Radiol Surg* 2023;18:1193–200.
- [123] Sun Y-K, Zhou B-Y, Miao Y, Shi Y-L, Xu S-H, Wu D-M, et al. Three-dimensional convolutional neural network model to identify clinically significant prostate cancer in transrectal ultrasound videos: a prospective, multiinstitutional, diagnostic study. *Eclinicalmedicine* 2023;60:102027.
- [124] Wilson PF, Gilany M, Jamzad A, Fooladgar F, To MNN, Wodlinger B, et al. Self-supervised learning with limited labeled data for prostate cancer detection in high frequency ultrasound. *IEEE Trans Ultrason Ferroelect Freq Control* 2023;70:1073–83.
- [125] Wu H, Fu J, Ye H, Zhong Y, Zhou X, Zhou J, et al. Multimodality transrectal ultrasound video classification for identification of clinically significant prostate cancer. 2024 IEEE 21st International Symposium on Biomedical Imaging. IEEE; 2024. p. 1–5.
- [126] Wu H, Fu J, Ye H, Zhong Y, Zhou X, Zhou J, et al. Towards multi-modality fusion and prototype-based feature refinement for clinically significant prostate cancer classification in transrectal ultrasound. *Medical Image Computing and Computer Assisted Intervention*. New York: Springer; 2024. p. 724–33.
- [127] Choi M, Zhou S, Kornberg Z, Sommer E, Fan R, Brooks J, et al. MIC-CUSP: Multi-modal image correlations for ultrasound-based prostate cancer detection. *Simplifying Medical Ultrasound: 4th International Workshop, ASMUS 2023, Held in Conjunction with MICCAI 2023, 14337*. New York: Springer Nature; 2023. p. 121.
- [128] Wei Z, Gardi L, Downey DB, Fenster A. Oblique needle segmentation and tracking for 3D TRUS-guided prostate brachytherapy. *Med Phys* 2005;32:2928–41.
- [129] Wayne M, Rossa C, Sloboda R, Usmani N, Tavakoli M. Three-dimensional needle shape estimation in TRUS-guided prostate brachytherapy using 2-D ultrasound images. *IEEE J Biomed Health Inform* 2015;20:1621–31.
- [130] Cool DW, Gardi L, Romagnoli C, Saikaly M, Izawa JI, Fenster A. Temporal-based needle segmentation algorithm for transrectal ultrasound prostate biopsy procedures. *Med Phys* 2010;37:1660–73.
- [131] Qiu W, Yuchi M, Ding M, Tessier D, Fenster A. Needle segmentation using 3d hough transform in 3D TRUS guided prostate transperineal therapy. *Med Phys* 2013;40:042902.
- [132] Qiu W, Yuchi M, Ding M. Phase grouping-based needle segmentation in 3-D transrectal ultrasound-guided prostate trans-perineal therapy. *Ultrasound Med Biol* 2014;40:804–16.
- [133] Wang F, Xing L, Bagshaw H, Buyyounouski M, Han B. Deep learning applications in automatic needle segmentation in ultrasound-guided prostate brachytherapy. *Med Phys* 2020;47:3797–805.
- [134] Zhang Y, Harms J, Lei Y, Wang T, Liu T, Jani AB, et al. Weakly supervised multi-needle detection in 3D ultrasound images with bidirectional convolutional sparse coding. *Medical Imaging 2020: Ultrasonic Imaging and Tomography*, 11319. Bellingham WA: SPIE; 2020. p. 229–36.
- [135] Zhang Y, Tian Z, Lei Y, Wang T, Patel P, Jani AB, et al. Automatic multi-needle localization in ultrasound images using large margin mask RCNN for ultrasound-guided prostate brachytherapy. *Phys Med Biol* 2020;65:205003.
- [136] Zhang Y, He X, Tian Z, Jeong JJ, Lei Y, Wang T, et al. Multi-needle detection in 3D ultrasound images using unsupervised order-graph regularized sparse dictionary learning. *IEEE Trans Med Imag* 2020;39:2302–15.
- [137] Richard WD, Keen CG. Automated texture-based segmentation of ultrasound images of the prostate. *Comput Med Imaging Graph* 1996;20:131–40.
- [138] Liu Y, Ng W, Teo M, Lim H. Computerised prostate boundary estimation of ultrasound images using radial bas-relief method. *Med Biol Engin Comput* 1997;35:445–54.
- [139] Kwok C, Teo M, Ng W, Tan S, Jones L. Outlining the prostate boundary using the harmonics method. *Med Biol Engin Comput* 1998;36:768–71.
- [140] Aarnink R, Pathak SD, De La Rosette JJ, Debruyne FM, Kim Y, et al. Edge detection in prostatic ultrasound images using integrated edge maps. *Ultrasonics* 1998;36:635–42.
- [141] Ladak HM, Mao F, Wang Y, Downey DB, Steinman DA, Fenster A. Prostate segmentation from 2d ultrasound images. In: *Proceedings of the 22nd Annual International Conference of the IEEE Engineering in Medicine and Biology Society (Cat. No. 00CH37143)*. New York: IEEE; 2000. p. 3188–91.
- [142] Liu H, Cheng G, Rubens D, Strang JG, Liao L, Brasacchio R, et al. Automatic segmentation of prostate boundaries in transrectal ultrasound (TRUS) imaging. *Medical Imaging 2002: Image Processing*, 4684. Bellingham WA: SPIE; 2002. p. 412–23.
- [143] Abolmaesumi R, Sirouspour MR. Segmentation of prostate contours from ultrasound images. *IEEE International Conference on Acoustics, Speech, and Signal Processing*. New York: IEEE; 2004.
- [144] Jendoubi A, Zeng J, Chouikha MF. Segmentation of prostate ultrasound images using an improved snakes model. In: *Proceedings 7th International Conference on Signal Processing*, 2004. New York: IEEE; 2004. p. 2568–71.
- [145] Sahba F, Tizhoosh HR, Salama MM. Segmentation of prostate boundaries using regional contrast enhancement. *IEEE International Conference on Image Processing* 2005. New York: IEEE; 2005.
- [146] Betrouni N, Vermandel M, Pasquier D, Maouche S, Rousseau J. Segmentation of abdominal ultrasound images of the prostate using a priori information and an adapted noise filter. *Comput Med Imaging Graph* 2005;29:43–51.
- [147] Zaim A. Automatic segmentation of the prostate from ultrasound data using feature-based self organizing map. *Image Analysis: 14th Scandinavian Conference, SCIA 2005*. New York: Springer; 2005. p. 1259–65.
- [148] Zhan Y, Shen D. Increasing efficiency of SVM by adaptively penalizing outliers. *International Workshop on Energy Minimization Methods in Computer Vision and Pattern Recognition*. New York: Springer; 2005. p. 539–51.
- [149] Medina R, Bravo A, Windyga P, Toro J, Yan P, Onik G. A 2-D active appearance model for prostate segmentation in ultrasound images. 2005 IEEE Engineering in Medicine and Biology 27th Annual Conference. New York: IEEE; 2006. p. 3363–6.
- [150] Hodge AC, Fenster A, Downey DB, Ladak HM. Prostate boundary segmentation from ultrasound images using 2D active shape models: Optimisation and extension to 3D. *Comput Methods Programs Biomed* 2006;84::99–113.
- [151] Kachouie NN, Fieguth P, Rahnamayan S. An elliptical level set method for automatic TRUS prostate image segmentation. 2006 IEEE International Symposium on Signal Processing and Information Technology. New York: IEEE; 2006. p. 191–6.
- [152] Mohamed S, Youssef AM, El-Saadany E, Salama MM. Prostate tissue characterization using TRUS image spectral features. *Image Analysis and Recognition: Third International Conference, ICIAR 2006*. New York: Springer; 2006. p. 589–601.
- [153] Zaim A, Jankun J. An energy-based segmentation of prostate from ultrasound images using dot-pattern select cells. 2007 IEEE International Conference on Acoustics, Speech and Signal Processing/ICASSP'07. New York: IEEE; 2007.
- [154] Kachouie NN, Fieguth P. A medical texture local binary pattern for TRUS prostate segmentation. 2007 29th Annual International Conference of the IEEE Engineering in Medicine and Biology Society. New York: IEEE; 2007. p. 5605–8.
- [155] Zaim A, Yi T, Keck R. Feature-based classification of prostate ultrasound images using multiwavelet and kernel support vector machines. 2007 International Joint Conference on Neural Networks. New York: IEEE; 2007. p. 278–81.
- [156] Saroul L, Bernard O, Vray D, Friboulet D. Prostate segmentation in echographic images: A variational approach using deformable super-ellipse and rayleigh distribution. 2008 5th IEEE International Symposium on Biomedical Imaging: From Nano to Macro. New York: IEEE; 2008. p. 129–32.
- [157] Zouqi M, Samarabandu J. Prostate segmentation from 2-D ultrasound images using graph cuts and domain knowledge. 2008 Canadian Conference on Computer and Robot Vision. New York: IEEE; 2008. p. 359–62.
- [158] Diaz K, Castaneda B. Semi-automated segmentation of the prostate gland boundary in ultrasound images using a machine learning approach. *Medical Imaging 2008: Image Processing*, 6914. Bellingham WA: SPIE; 2008. p. 1364–71.
- [159] Ghose S, Oliver A, Martí R, Lladó X, Freixenet J, Vilanova JC, et al. Texture guided active appearance model propagation for prostate segmentation. *Prostate Cancer Imaging. Computer-Aided Diagnosis, Prognosis, and Intervention: International Workshop, Held in Conjunction with MICCAI 2010*. New York: Springer; 2010. p. 111–20.
- [160] Xu RS, Michailovich O, Salama M. Information tracking approach to segmentation of ultrasound imagery of the prostate. *IEEE Trans Ultrason Ferroelect Freq Control* 2010;57:1748–61.
- [161] Ghose S, Oliver A, Martí R, Lladó X, Freixenet J, Mitra J, et al. Multiple mean models of statistical shape and probability priors for automatic prostate segmentation. *Prostate Cancer Imaging. Image Analysis and Image-Guided Interventions: International Workshop, Held in Conjunction with MICCAI 2011*. New York: Springer; 2011. p. 35–46.
- [162] Hassanien AE, Al-Qaheri H, El-Dahshan E-SA. Prostate boundary detection in ultrasound images using biologically-inspired spiking neural network. *Appl Soft Comput* 2011;11:2035–41.
- [163] Ghose S, Oliver A, Martí R, Lladó X, Freixenet J, Vilanova JC, et al. A probabilistic framework for automatic prostate segmentation with a statistical model of shape and appearance. 2011 18th IEEE International Conference on Image Processing. New York: IEEE; 2011. p. 713–6.
- [164] Ghose S, Oliver A, Martí R, Lladó X, Freixenet J, Vilanova JC, et al. Prostate segmentation with local binary patterns guided active appearance models. *Medical Imaging 2011: Image Processing*, 7962. Bellingham WA: SPIE; 2011. p. 389–96.
- [165] Manavalan R, Thangavel K. TRUS image segmentation using morphological operators and DBSCAN clustering. 2011 World Congress on information and communication technologies. New York: IEEE; 2011. p. 898–903.
- [166] Ghose S, Oliver A, Martí R, Lladó X, Freixenet J, Mitra J, et al. Statistical shape and texture model of quadrature phase information for prostate segmentation. *Int J Comput Assist Radiol Surg* 2012;7:43–55.
- [167] Ghose S, Oliver A, Martí R, Lladó X, Freixenet J, Mitra J, et al. Statistical shape and texture model of quadrature phase information for prostate segmentation. *Int J Comput Assist Radiol Surg* 2012;7:43–55.
- [168] Ghose S, Mitra J, Oliver A, Martí R, Lladó X, Freixenet J, et al. A supervised learning framework for automatic prostate segmentation in trans rectal ultrasound images. *Advanced Concepts for Intelligent Vision Systems: 14th International Conference, ACIVS 2012*. New York: Springer; 2012. p. 190–200.
- [169] Vafaei R, Alirezaie J, Babyn P. A fast model-based prostate boundary segmentation using normalized cross-correlation and representative patterns in ultrasound images. 2012 IEEE-EMBS Conference on Biomedical Engineering and Sciences. New York: IEEE; 2012. p. 723–7.
- [170] Eskandari H, Talebpour A, Tabrizi SH, Nowroozi MR. Development of a fast algorithm for automatic delineation of prostate gland on 2D ultrasound images. 2012 19th Iranian Conference of Biomedical Engineering. New York: IEEE; 2012. p. 313–7.
- [171] Vafaei R, Alirezaie J, Babyn P. Fully automated model-based prostate boundary segmentation using Markov random field in ultrasound images. 2012 International Conference on Digital Image Computing Techniques and Applications. New York: IEEE; 2012. p. 1–8.
- [172] Yu Y, Chen Y, Chiu B. Fully automatic prostate segmentation from transrectal ultrasound images based on radial bas-relief initialization and slice-based propagation. *Comput Biol Med* 2016;74:74–90.
- [173] Li X, Li C, Fedorov A, Kapur T, Yang X. Segmentation of prostate from ultrasound images using level sets on active band and intensity variation across edges. *Med Phys* 2016;43:3090–103.
- [174] Zeng Q, Samei G, Karimi D, Kesck C, Mahdavi SS, Abolmaesumi P, et al. Prostate segmentation in transrectal ultrasound using magnetic resonance imaging priors. *Int J Comput Assist Radiol Surg* 2018;13:749–57.

- [175] Georgieva V, Mihaylova A, Petrov P. Prostate segmentation in ultrasound images using hybrid method. 2018 International Conference on High Technology for Sustainable Development. New York: IEEE; 2018. p. 1–4.
- [176] Anas EMA, Mousavi P, Abolmaesumi P. A deep learning approach for real time prostate segmentation in freehand ultrasound guided biopsy. *Med Image Anal* 2018;48:107–16.
- [177] Van Sloun R, Wildeboer R, Postema A, Mannaerts C, Gayer M, Wijkstra H, et al. Zonal segmentation in transrectal ultrasound images of the prostate through deep learning. 2018 IEEE International Ultrasonics Symposium. New York: IEEE; 2018. p. 1–4.
- [178] Orlando N, Gillies DJ, Gyacskov I, Romagnoli C, DSouza D, Fenster A. Automatic prostate segmentation using deep learning on clinically diverse 3D transrectal ultrasound images. *Med Phys* 2020;47:2413–26.
- [179] Geng L, Li S, Xiao Z, Zhang F. Multi-channel feature pyramid networks for prostate segmentation, based on transrectal ultrasound imaging. *Appl Sci* 2020;10:3834.
- [180] Peng T, Zhao J, Wang J. Interpretable mathematical model-guided ultrasound prostate contour extraction using data mining techniques. 2021 IEEE International Conference on Bioinformatics and Biomedicine. New York: IEEE; 2021. p. 1037–44.
- [181] Beitone C, Troccaz J. Multi-expert fusion: An ensemble learning framework to segment 3D TRUS prostate images. *Med Phys* 2022;49:5138–48.
- [182] Bi H, Sun J, Jiang Y, Ni X, Shu H. Structure boundary-preserving u-net for prostate ultrasound image segmentation. *Front Oncol* 2022;12:900340.
- [183] Peng T, Wu Y, Cai J. Improving the detection of the prostate in ultrasound images using machine learning based image processing. 2022 IEEE 19th International Symposium on Biomedical Imaging. New York: IEEE; 2022. p. 1–4.
- [184] Peng T, Zhao J, Gu Y, Wang C, Wu Y, Cheng X, et al. HProMed: Ultrasound image segmentation based on the evolutionary neural network and an improved principal curve. *Pattern Recognit* 2022;131:108890.
- [185] Peng T, Tang C, Wang J. Prostate segmentation of ultrasound images based on interpretable-guided mathematical model. International Conference on Multimedia Modeling. New York: Springer; 2022. p. 166–77.
- [186] Peng T, Wu Y, Qin J, Wu QJ, Cai J. H-ProSeg: Hybrid ultrasound prostate segmentation based on explainability-guided mathematical model. *Comput Methods Programs Biomed* 2022;219:106752.
- [187] Carriere J, Sloboda R, Usmani N, Tavakoli M. Autonomous prostate segmentation in 2D B-mode ultrasound images. *Appl Sci* 2022;12:2994.
- [188] Peng T, Zhao J, Xu Y, Cai J. Combining an optimized closed principal curve-based method and evolutionary neural network for ultrasound prostate segmentation. *Int J Electron Commun Eng* 2022;16:131–6.
- [189] Peng T, Tang C, Wu Y, Cai J. Semi-automatic prostate segmentation from ultrasound images using machine learning and principal curve based on interpretable mathematical model expression. *Front Oncol* 2022;12:878104.
- [190] Yi W, Stavrinides V, Baum ZM, Yang Q, Barratt DC, Clarkson MJ, et al. Boundary-RL: Reinforcement learning for weakly-supervised prostate segmentation in TRUS images. International Workshop on Machine Learning in Medical Imaging. New York: Springer; 2023. p. 277–88.
- [191] Peng T, Dong Y, Di G, Zhao J, Li T, Ren G, et al. Boundary delineation in transrectal ultrasound images for region of interest of prostate. *Phys Med Biol* 2023;68:195008.
- [192] Peng T, Zhang Y, Dong Y, Ruan Y, Jin R, Liu Z, et al. AI-based intelligent-annotation algorithm for medical segmentation from ultrasound data. Pacific Rim International Conference on Artificial Intelligence. New York: Springer; 2023. p. 28–40.
- [193] Peng T, Wu Y, Gu Y, Xu D, Wang C, Li Q, et al. Intelligent contour extraction approach for accurate segmentation of medical ultrasound images. *Front Physiol* 2023;14:1177351.
- [194] Peng T, Xu D, Tang C, Zhao J, Shen Y, Yang C, et al. Automatic coarse-to-refine-based ultrasound prostate segmentation using optimal polyline segment tracking method and deep learning. *Appl Intell* 2023;53:21390–406.
- [195] Peng T, Wu Y, Zhao J, Wang C, Wang J, Cai J. Ultrasound prostate segmentation using adaptive selection principal curve and smooth mathematical model. *J Digit Imaging* 2023;36:947–63.
- [196] Feng Y, Atabansi CC, Nie J, Liu H, Zhou H, Zhao H, et al. Multi-stage fully convolutional network for precise prostate segmentation in ultrasound images. *Biocybernet Biomed Eng* 2023;43:586–602.
- [197] Peng T, Xu D, Wu Y, Zhao J, Mao H, Cai J, et al. Delineation of prostate boundary from medical images via a mathematical formula-based hybrid algorithm. International Conference on Artificial Neural Networks. New York: Springer; 2023. p. 160–71.
- [198] Ghavami N, Hu Y, Bonmati E, Rodell R, Gibson E, Moore C, et al. Integration of spatial information in convolutional neural networks for automatic segmentation of intraoperative transrectal ultrasound images. *J Med Imag* 2019;6 011003-011003.
- [199] Liu C, Dong G, Lin M, Zou Y, Liang T, He X, et al. ARS-Net: Adaptively rectified supervision network for automated 3D ultrasound image segmentation. *Medical Image Computing and Computer Assisted Intervention-MICCAI* 2019. New York: Springer; 2019. p. 375–83.
- [200] Ghanei A, Soltanian-Zadeh H, Ratkiewicz A, Yin F-F. A three-dimensional deformable model for segmentation of human prostate from ultrasound images. *Med Phys* 2001;28:2147–53.
- [201] Hu N, Downey DB, Fenster A, Ladak HM. Prostate surface segmentation from 3D ultrasound images. In: Proceedings IEEE International Symposium on Biomedical Imaging. New York: IEEE; 2002. p. 613–6.
- [202] Ding M, Chen C, Wang Y, Gyacskov I, Fenster A. Prostate segmentation in 3D US images using the cardinal-spline-based discrete dynamic contour. *Medical Imaging 2003: Visualization, Image-Guided Procedures, and Display*, 5029. Bellingham WA: SPIE; 2003. p. 69–76.
- [203] Zhan Y, Shen D. An efficient method for deformable segmentation of 3D US prostate images. International Workshop on Medical Imaging and Virtual Reality. New York: Springer; 2004. p. 103–12.
- [204] Ding M, Gyacskov I, Yuan X, Drangova M, Fenster A, Downey D. Slice-based prostate segmentation in 3D US images using continuity constraint. 2005 IEEE Engineering in Medicine and Biology. New York: IEEE; 2006. p. 662–5.
- [205] Yang F, Suri J, Fenster A. Segmentation of prostate from 3-D ultrasound volumes using shape and intensity priors in level set framework. 2006 International Conference of the IEEE Engineering in Medicine and Biology Society. New York: IEEE; 2006. p. 2341–4.
- [206] Akbari H, Yang X, Halig L V, Fei B. 3D segmentation of prostate ultrasound images using wavelet transform. *Medical Imaging 2011: Image Processing*, 7962. Bellingham WA: SPIE; 2011. p. 812–7.
- [207] Yang X, Schuster D, Master V, Nieh P, Fenster A, Fei B. Automatic 3D segmentation of ultrasound images using atlas registration and statistical texture prior. *Medical Imaging 2011: Visualization, Image-Guided Procedures, and Modeling*, 7964. Bellingham WA: SPIE; 2011. p. 912–8.
- [208] Yang X, Fei B. 3D prostate segmentation of ultrasound images combining longitudinal image registration and machine learning. *Medical Imaging 2012: Image-Guided Procedures, Robotic Interventions, and Modeling*, 8316. Bellingham WA: SPIE; 2012. p. 803–11.
- [209] Yu Y, Cheng J, Li J, Chen W, Chiu B. Automatic prostate segmentation from transrectal ultrasound images. 2014 IEEE Biomedical Circuits and Systems Conference (BioCAS) Proceedings. New York: IEEE; 2014. p. 117–20.
- [210] Ma L, Guo R, Tian Z, Venkataraman R, Sarkar S, Liu X, et al. Random walk based segmentation for the prostate on 3D transrectal ultrasound images. *Medical Imaging 2016: Image-Guided Procedures, Robotic Interventions, and Modeling*, 9786. Bellingham WA: SPIE; 2016. p. 75–82.
- [211] Ma L, Guo R, Tian Z, Fei B. A random walk-based segmentation framework for 3D ultrasound images of the prostate. *Med Phys* 2017;44:5128–42.
- [212] Lei Y, Wang T, Wang B, He X, Tian S, Jani AB, et al. Ultrasound prostate segmentation based on 3D V-net with deep supervision. *Medical Imaging 2019: Ultrasonic Imaging and Tomography*, 10955. Bellingham WA: SPIE; 2019. p. 198–204.
- [213] Liu M, Wu K, Jiang L. ADC-Net: adaptive detail compensation network for prostate segmentation in 3D transrectal ultrasound images. *Medical Imaging 2023: Ultrasonic Imaging and Tomography*, 12470. Bellingham WA: SPIE; 2023. p. 211–20.
- [214] Knoll C, Alcañiz M, Grau V, Monserrat C, Juan MC. Outlining of the prostate using snakes with shape restrictions based on the wavelet transform (doctoral thesis: Dissertation). *Pattern Recognit* 1999;32:1767–81.
- [215] Yang X, Akbari H, Halig L, Fei B. 3D non-rigid registration using surface and local salient features for transrectal ultrasound image-guided prostate biopsy. *Medical Imaging 2011: Visualization, Image-Guided Procedures, and Modeling*, 7964. Bellingham WA: SPIE; 2011. p. 863–70.
- [216] Khallaghi S, Sánchez CA, Nouranian S, Sojoudi S, Chang S, Abdi H, et al. A 2D3D registration framework for freehand TRUS-guided prostate biopsy. *Medical Image Computing and Computer Assisted Intervention-MICCAI* 2015. New York: Springer; 2015. p. 272–9.
- [217] Figl M, Hoffmann R, Kaar M, Hummel J. Deformable registration of 3D ultrasound volumes using automatic landmark generation. *PLoS One* 2019;14:e0213004.
- [218] Zhu N, Najafi M, Han B, Hancock S, Hristov D. Feasibility of image registration for ultrasound-guided prostate radiotherapy based on similarity measurement by a convolutional neural network. *Technol Cancer Res Treat* 2019;18:153303 3818821964.
- [219] Dupuy T, Beitone C, Troccaz J, Voros S. 2D/3D deep registration for real-time prostate biopsy navigation. *Medical Imaging 2021: Image-Guided Procedures, Robotic Interventions, and Modeling*, 11598. Bellingham WA: SPIE; 2021. p. 463–71.
- [220] Fang Z, Delingette H, Ayache N. Anatomical landmark detection for initializing US and MR image registration. International Workshop on Advances in Simplifying Medical Ultrasound. New York: Springer; 2023. p. 165–74.
- [221] Mizowaki T, Gilad N C, Fung AY, Zaider M. Towards integrating functional imaging in the treatment of prostate cancer with radiation: the registration of the MR spectroscopy imaging to ultrasound/CT images and its implementation in treatment planning. *Int J Radiat Oncol Biol Phys* 2002;54:1558–64.
- [222] Sun Y, Yuan J, Rajchl M, Qiu W, Romagnoli C, Fenster A. Efficient convex optimization approach to 3D non-rigid MR-TRUS registration. *Medical Image Computing and Computer Assisted Intervention-MICCAI* 2013. New York: Springer; 2013. p. 195–202.
- [223] van de Ven WJ, Hu Y, Barentsz JO, Karssemeijer N, Barratt D, Huisman HJ. Surface-based prostate registration with biomechanical regularization. *Medical Imaging 2013: Image-Guided Procedures, Robotic Interventions, and Modeling*, 8671. Bellingham WA: SPIE; 2013. p. 447–52.
- [224] Wang Y, Ni D, Qin J, Yang X, Xie X, Lin M, et al. Personalized modeling of prostate deformation based on elastography for MRI-TRUS registration. 2014 IEEE 11th International Symposium on Biomedical Imaging. New York: IEEE; 2014. p. 782–5.
- [225] Wang Y, Ni D, Qin J, Lin M, Xie X, Xu M, et al. Towards personalized biomechanical model and MIND-weighted point matching for robust deformable MR-TRUS registration. *Computer-Assisted and Robotic Endoscopy: First International Workshop, CARE 2014, Held in Conjunction with MICCAI* 2014. New York: Springer; 2014. p. 121–30.
- [226] Yang X, Rossi P, Mao H, Jani AB, Ogunleye T, Curran WJ, et al. A MR-TRUS registration method for ultrasound-guided prostate interventions. *Medical Imaging 2015: Image-Guided Procedures, Robotic Interventions, and Modeling*, 9415. Bellingham WA: SPIE; 2015. p. 482–90.
- [227] van de Ven WJ, Hu Y, Barentsz JO, Karssemeijer N, Barratt D, Huisman HJ. Biomechanical modeling constrained surface-based image registration for prostate MR guided TRUS biopsy. *Med Phys* 2015;42:2470–81.
- [228] Fedorov A, Khallaghi S, Sánchez CA, Lasso A, Fels S, Tuncali K, et al. Open-source image registration for MRI-TRUS fusion-guided prostate interventions. *Int J Comput Assist Radiol Surg* 2015;10:925–34.

- [229] Shakeri S, Menard C, Lopes R, Kadoury S. Deformable MRI-TRUS surface registration from statistical deformation models of the prostate. *Medical Imaging 2019: Image-Guided Procedures, Robotic Interventions, and Modeling*, 10951. Bellingham WA: SPIE; 2019. p. 504–10.
- [230] Mathur P, Samei G, Tsang K, Lobo J, Salcudean S. On the feasibility of transperineal 3D ultrasound image guidance for robotic radical prostatectomy. *Int J Comput Assist Radiol Surg* 2019;14:923–31.
- [231] Bhardwaj A, Park J-S, Mukhopadhyay S, Sharda S, Son Y, Ajani B, et al. Rigid and deformable corrections in realtime using deep learning for prostate fusion biopsy. *Medical Imaging 2020: Image-Guided Procedures, Robotic Interventions, and Modeling*, 11315. Bellingham WA: SPIE; 2020. p. 486–99.
- [232] Igarashi R, Koizumi N, Nishiyama Y, Tomita K, Shigenari Y, Shoji S. Sagittal alignment in an MR-TRUS fusion biopsy using only the prostate contour in the axial image. *ROBOMECH J* 2020;7:1–7.
- [233] Zeng Q, Fu Y, Jeong J, Lei Y, Wang T, Mao H, et al. Weakly non-rigid MR-TRUS prostate registration using fully convolutional and recurrent neural networks. *Medical Imaging 2020: Image Processing*, 11313. Bellingham WA: SPIE; 2020. p. 754–60.
- [234] Bashkanov O, Meyer A, Schindele D, Schostak M, Tonnies K-D, Hansen C, et al. Learning multi-modal volumetric prostate registration with weak inter-subject spatial correspondence. 2021 IEEE 18th International Symposium on Biomedical Imaging. New York: IEEE; 2021. p. 1817–21.
- [235] Baum ZM, Hu Y, Barratt DC. Meta-learning initializations for interactive medical image registration. *IEEE Trans Med Imag* 2022;42:823–33.
- [236] Castro-Pareja CR, Zagrodsky V, Bouchet L, Shekhar R. Automated prostate localization in external-beam radiotherapy using mutual information-based registration of treatment planning CT and daily 3D ultrasound images. *International Congress Series*. Elsevier; 2005. p. 435–40.
- [237] Fei B, Master V, Nieh P, Akbari H, Yang X, Fenster A, et al. A PET/CT directed, 3D ultrasound-guided biopsy system for prostate cancer. *Prostate Cancer Imaging. Image Analysis and Image-Guided Interventions: International Workshop, Held in Conjunction with MICCAI 2011*. New York: Springer; 2011. p. 100–8.
- [238] Sultana S, Song DY, Lee J. Deformable registration of PET/CT and ultrasound for disease-targeted focal prostate brachytherapy. *J Med Imag* 2019;6 035003-035003.
- [239] Lei Y, Wang T, Fu Y, Roper J, Jani AB, Liu T, et al. Catheter position prediction using deep-learning-based multi-atlas registration for high-dose rate prostate brachytherapy. *Med Phys* 2021;48:7261–70.
- [240] De Silva T, Cool D W, Yuan J, Romagnoli C, Samarabandu J, et al. Robust 2-D-3-D registration optimization for motion compensation during 3-D TRUS-guided biopsy using learned prostate motion data. *IEEE Trans Med Imag* 2017;36:2010–20.
- [241] Beerlage HP, Aarnink R G, Ruijter E, Witjes JA, Wijkstra H, van de Kaa CA, et al. Correlation of transrectal ultrasound, computer analysis of transrectal ultrasound and histopathology of radical prostatectomy specimen. *Prostate Cancer Prostat Dis* 2001;4:56–62.
- [242] Mohamed M, Abdel-Galil T, El-Saadany E, Fenster A, Downey D, Rizkalla K, et al. Prostate cancer diagnosis based on Gabor filter texture segmentation of ultrasound image. *CCECE 2003-Canadian Conference on Electrical and Computer Engineering. Toward a Caring and Humane Technology (Cat. No. 03CH37436)*. New York: IEEE; 2003. p. 1485–8.
- [243] Scheipers U, Ermet H, Sommerfeld H-J, Garcia-Schürmann M, Senge T, Philippou S. Ultrasonic multifeature tissue characterization for prostate diagnostics. *Ultrasound Med Biol* 2003;29:1137–49.
- [244] Feleppa EJ, Ketterling JA, Porter CR, Gillespie J, Wu C-S, Urban S, et al. Ultrasonic tissue-type imaging (TTI) for planning treatment of prostate cancer. *Medical Imaging 2004: Ultrasonic Imaging and Signal Processing*, 5373. Bellingham WA: SPIE; 2004. p. 223–30.
- [245] Llobet R, Pérez-Cortés JC, Toselli AH, Juan A. Computer-aided detection of prostate cancer. *Int J Med Inform* 2007;76:547–56.
- [246] Mohamed SS, Salama MM. Prostate cancer spectral multifeature analysis using TRUS images. *IEEE Trans Med Imag* 2008;27:548–56.
- [247] Fei B, Schuster DM, Master V, Akbari H, Fenster A, Nieh P. A molecular image-directed, 3D ultrasound-guided biopsy system for the prostate. *Medical Imaging 2012: Image-Guided Procedures, Robotic Interventions, and Modeling*, 8316. Bellingham WA: SPIE; 2012. p. 345–52.
- [248] Pareek G, Acharya UR, Sree SV, Swapna G, Yantri R, Martis RJ, et al. Prostate tissue characterization/classification in 144 patient population using wavelet and higher order spectra features from transrectal ultrasound images. *Technol Cancer Res Treat* 2013;12:545–57.
- [249] Huang X, Chen M, Liu P, Du Y, et al. Texture feature-based classification on transrectal ultrasound image for prostatic cancer detection. *Comput Math Methods Med* 2020;2020:7359375.
- [250] Liu Z, Yang C, Huang J, Liu S, Zhuo Y, Lu X. Deep learning framework based on integration of S-Mask R-CNN and Inception-v3 for ultrasound image-aided diagnosis of prostate cancer. *Future Generation Computer Systems* 2021;114:358–67.
- [251] Akatsuka J, Numata Y, Morikawa H, Sekine T, Kayama S, Mikami H, et al. A data-driven ultrasound approach discriminates pathological high grade prostate cancer. *Sci Rep* 2022;12:860.
- [252] Hassan MR, Islam M F, Uddin MZ, Ghoshal G, Hassan MM, et al. Prostate cancer classification from ultrasound and MRI images using deep learning based explainable artificial intelligence. *Future Generation Computer Systems* 2022;127:462–72.
- [253] Huang T-L, Lu N-H, Huang Y-H, Twan W-H, Yeh L-R, Liu KY, et al. Transfer learning with CNNs for efficient prostate cancer and BPH detection in transrectal ultrasound images. *Sci Rep* 2023;13:21849.
- [254] Wildeboer R, Postema A, Demi L, Kuenen M, Wijkstra H, Mischi M. Multiparametric dynamic contrast-enhanced ultrasound classification of prostate cancer. 2016 IEEE International Ultrasonics Symposium. New York: IEEE; 2016. p. 1–4.
- [255] Azizi S, Mousavi P, Yan P, Tahmasebi A, Kwak JT, Xu S, et al. Transfer learning from RF to B-mode temporal enhanced ultrasound features for prostate cancer detection. *Int J Comput Assist Radiol Surg* 2017;12:1111–21.
- [256] Sedghi A, Mehrash A, Jamzad A, Amalou A, Wells WM, Kapur T, Kwak JT, et al. Improving detection of prostate cancer focal foci via information fusion of MRI and temporal enhanced ultrasound. *Int J Comput Assist Radiol Surg* 2020;15:1215–23.
- [257] Fooladgar F, To MNN, Javadi G, Samadi S, Bayat S, Sojoudi S, et al. Uncertainty-aware deep ensemble model for targeted ultrasound-guided prostate biopsy. 2022 IEEE 19th International Symposium on Biomedical Imaging. New York: IEEE; 2022. p. 1–5.
- [258] Wildeboer R, Mannaerts CK, van Sloun R, Wijkstra H, Salomon G, Mischi M. Machine learning for multiparametric ultrasound classification of prostate cancer using B-mode, shear-wave elastography, and contrast-enhanced ultrasound radio-mics. 2019 IEEE International Ultrasonics Symposium. New York: IEEE; 2019. p. 1902–5.
- [259] Ding M, Fenster A. Projection-based needle segmentation in 3D ultrasound images. *Comput Aided Surg* 2004;9:193–201.
- [260] Krefting D, Haupt B, Tolxdorff T, Kempkensteffen C, Miller K. Segmentation of prostate biopsy needles in transrectal ultrasound images. *Medical Imaging 2007: Image Processing*, 6512. Bellingham WA: SPIE; 2007. p. 1001–8.
- [261] Ayvaci A, Yan P, Xu S, Soatto S, Kruecker J. Biopsy needle detection in transrectal ultrasound. *Comput Med Imaging Graph* 2011;35:653–9.
- [262] Tang C, Xie G, Omisore O M, Xiong J, Xia Z. A real-time needle tracking algorithm with first-frame linear structure removing in 2D ultrasound-guided prostate therapy. 2019 IEEE International Conference on Robotics and Biomimetics. New York: IEEE; 2019. p. 1240–5.
- [263] Mukhopadhyay S, Mathur P, Bharadwaj A, Son Y, Park J-S, Kudavelly SR, Song S, et al. Deep learning-based needle tracking in prostate fusion biopsy. *Medical Imaging 2021: Image-Guided Procedures, Robotic Interventions, and Modeling*, 11598. Bellingham WA: SPIE; 2021. p. 605–13.
- [264] Wei Z, Gardi L, Downey DB, Fenster A. Oblique needle segmentation for 3D TRUS-guided robot-aided transperineal prostate brachytherapy. 2004 2nd IEEE International Symposium on Biomedical Imaging: Nano to Macro. New York: IEEE; 2004. p. 960–3.
- [265] Ding M, Wei Z, Gardi L, Downey DB, Fenster A. Needle and seed segmentation in intra-operative 3D ultrasound-guided prostate brachytherapy. *Ultrasonics* 2006;44: e331–6.
- [266] Yan P, Cheeseborough III JC, Chao KC. Automatic shape-based level set segmentation for needle tracking in 3-D TRUS-guided prostate brachytherapy. *Ultrasound Med Biol* 2012;38:1626–36.
- [267] Buzurovic I, Misic V, Yu Y. Needle identification in high-dose-rate prostate brachytherapy using ultrasound imaging modality. 2012 Annual International Conference of the IEEE Engineering in Medicine and Biology Society. New York: IEEE; 2012. p. 476–9.
- [268] Waïne M, Rossa C, Sloboda R, Usmani N, Tavakoli M. 3D shape visualization of curved needles in tissue from 2D ultrasound images using RANSAC. 2015 IEEE International Conference on Robotics and Automation. New York: IEEE; 2015. p. 4723–8.
- [269] Hrinivich WT, Hoover DA, Surry K, Edirisinghe C, Montreuil J, et al. Simultaneous automatic segmentation of multiple needles using 3D ultrasound for high-dose-rate prostate brachytherapy. *Med Phys* 2017;44:1234–45.
- [270] Younes H, Voros S, Troccaz J. Automatic needle localization in 3D ultrasound images for brachytherapy. 2018 IEEE 15th International Symposium on Biomedical Imaging. New York: IEEE; 2018. p. 1203–7.
- [271] Zhang Y, Lei Y, Qiu RL, Wang T, Wang HJani AB, et al. Multi-needle localization with attention U-net in US-guided HDR prostate brachytherapy. *Med Phys* 2020;47:2735–45.
- [272] Zhang Y, He X, Tian Z, Jeong J, Lei Y, Wang T, et al. Multi-needle detection in 3D ultrasound images with sparse dictionary learning. *Medical Imaging 2020: Ultrasonic Imaging and Tomography*, 11319. Bellingham WA: SPIE; 2020. p. 97–104.
- [273] Zhang Y, Lei Y, He X, Tian Z, Jeong J, Wang T, et al. Ultrasound multi-needle detection using deep attention U-net with TV regularizations. *Medical Imaging 2021: Image-Guided Procedures, Robotic Interventions, and Modeling*, 11598. Bellingham WA: SPIE; 2021. p. 599–604.
- [274] Zhang Y, Tian Z, Lei Y, Wang T, Patel P, Jani AB, et al. Multi-needle detection in ultrasound image using max-margin mask R-CNN. *Medical Imaging 2021: Ultrasonic Imaging and Tomography*, 11602. Bellingham WA: SPIE; 2021. p. 264–9.